Dark Energy Survey Year 1 Results: Methodology and Projections for Joint Analysis of Galaxy Clustering, Galaxy Lensing, and CMB Lensing Two-point Functions

E. Baxter[1], Y. Omori[2,3,4], C. Chang[5], T. Giannantonio[6,7,8], D. Kirk[9], E. Krause[10,11], J. Blazek[12,13], L. Bleem[14,15], A. Choi[17,18], T. M. Crawford[5,19], S. Dodelson[20], T. F. Eifler[10,11], O. Friedrich[8,51], D. Gruen[21,22], G. P. Holder[23,24,25], B. Jain[1], M. Jarvis[1], N. MacCrann[12,26], A. Nicola[27], S. Pandey[1], J. Prat[28], C. L. Reichardt[29], S. Samuroff[30], C. Sánchez[1,28], L. F. Secco[1], E. Sheldon[31], M. A. Troxel[12,26], J. Zuntz[32], T. M. C. Abbott[33], F. B. Abdalla[9,34], J. Annis[16], S. Avila[35], K. Bechtol[36], B. A. Benson[16,5,19], E. Bertin[37,38], D. Brooks[9], E. Buckley-Geer[16], D. L. Burke[21,22], A. Carnero Rosell[39,40], M. Carrasco Kind[41,42], J. Carretero[28], F. J. Castander[43,44], R. Cawthon[5], C. E. Cunha[21], C. B. D'Andrea[1], L. N. da Costa[39,40], C. Davis[21], J. De Vicente[45], D. L. DePoy[46], H. T. Diehl[16], P. Doel[9], J. Estrada[16], A. E. Evrard[47,48], B. Flaugher[16], P. Fosalba[43,44], J. Frieman[16,5], J. García-Bellido[49], E. Gaztanaga[43,44], D. W. Gerdes[47,48], R. A. Gruendl[41,42], J. Gschwend[39,40], G. Gutierrez[16], W. G. Hartley[9,27], D. Hollowood[50], B. Hoyle[51,8], D. J. James[52], S. Kent[16,5], K. Kuehn[53], N. Kuropatkin[16], O. Lahav[9], M. Lima[54,39], M. A. G. Maia[39,40], M. March[1], J. L. Marshall[46], P. Melchior[55], F. Menanteau[41,42], R. Miquel[56,28], A. A. Plazas[11], A. Roodman[21,22], E. S. Rykoff[21,22], E. Sanchez[45], R. Schindler[22], M. Schubnell[48], I. Sevilla-Noarbe[45], M. Smith[57], R. C. Smith[33], M. Soares-Santos[58], F. Sobreira[59,39], E. Suchyta[60], M. E. C. Swanson[42], G. Tarle[48], A. R. Walker[33], W. L. K. Wu[5], J. Weller[61,51,8]

Author affiliations are listed at the end of this paper

15 February 2018

ABSTRACT

Optical imaging surveys measure both the galaxy density and the gravitational lensing-induced shear fields across the sky. Recently, the Dark Energy Survey (DES) collaboration used a joint fit to two-point correlations between these observables to place tight constraints on cosmology (DES Collaboration et al. 2017). In this work, we develop the methodology to extend the DES Collaboration et al. (2017) analysis to include cross-correlations of the optical survey observables with gravitational lensing of the cosmic microwave background (CMB) as measured by the South Pole Telescope (SPT) and *Planck*. Using simulated analyses, we show how the resulting set of five two-point functions increases the robustness of the cosmological constraints to systematic errors in galaxy lensing shear calibration. Additionally, we show that contamination of the SPT+*Planck* CMB lensing map by the thermal Sunyaev-Zel'dovich effect is a potentially large source of systematic error for two-point function analyses, but show that it can be reduced to acceptable levels in our analysis by masking clusters of galaxies and imposing angular scale cuts on the two-point functions. The methodology developed here will be applied to the analysis of data from the DES, the SPT, and *Planck* in a companion work.

1 INTRODUCTION

Modern optical imaging surveys measure the positions and gravitational lensing-induced shears of millions of galaxies. From these measurements, one can compute two fields on the sky: the spin-0 galaxy overdensity field, δ_g, and the spin-2 weak lensing shear field, γ. Two-point cross-correlations between these fields are powerful cosmological probes, as they are sensitive to both the geometry of the Universe and the growth of structure. Joint fits to multiple two-point correlations — such as $w^{\delta_g\delta_g}(\theta)$ and $w^{\delta_g\gamma}(\theta)$ — offer the possibility of breaking degeneracies between cosmological and nuisance parameters, as well as significantly improving cosmological constraints (e.g. Hu & Jain 2004).[1] Such joint fits have recently been demonstrated in several works (Nicola et al. 2016; Kwan et al. 2017; van Uitert et al. 2017; DES Collaboration et al. 2017). We refer to the set of three two-point functions that can be formed from γ and δ_g — namely $w^{\delta_g\delta_g}(\theta)$, $w^{\delta_g\gamma}(\theta)$, and $w^{\gamma\gamma}(\theta)$ — as 3×2pt. The 3×2pt analysis of the DES Collaboration et al. (2017) presented the tightest cosmological constraints to date on $\Omega_{\rm m}$ and $S_8 = \sigma_8\sqrt{\Omega_{\rm m}/0.3}$ from a single galaxy survey data set, demonstrating the power of such joint two-point correlation analyses.

High resolution, low-noise observations of the cosmic microwave background (CMB) have recently enabled mapping of gravitational lensing of the CMB, typically quantified via the lensing convergence, $\kappa_{\rm CMB}$. While it is possible to convert a map of the convergence to shear, doing so is not necessary for this analysis. Two-point functions that correlate $\kappa_{\rm CMB}$ with the δ_g and γ fields also contain cosmological information (Hand et al. 2015; Liu et al. 2016; Kirk et al. 2016; Harnois-Déraps et al. 2017; Giannantonio et al. 2016). Jointly fitting $w^{\gamma\kappa_{\rm CMB}}(\theta)$ and $w^{\delta_g\kappa_{\rm CMB}}(\theta)$ with the 3×2pt cross-correlations serves several purposes. First, the joint fit helps improve cosmological constraints by breaking degeneracies with galaxy bias (e.g. Baxter et al. 2016). Second, the joint fit can constrain nuisance parameters associated with sources of systematic error in galaxy lensing measurements (e.g. Vallinotto 2012; Das et al. 2013; Baxter et al. 2016; Schaan et al. 2017). This is possible because the sources of systematic error that affect the measurement of $\kappa_{\rm CMB}$ are generally different from those impacting the measurement of γ. Finally, because the CMB originates from high redshift, including the $\kappa_{\rm CMB}$ correlations extends the redshift lever arm of the two-point function measurements (e.g. Das & Spergel 2009).

The South Pole Telescope (SPT) (Carlstrom et al. 2011) and *Planck* (Tauber et al. 2010; Planck Collaboration et al. 2011) provide high signal-to-noise maps of the CMB overlapping with the DES survey, allowing for the joint measurement of all six of the two-point functions that can be formed from δ_g, γ and $\kappa_{\rm CMB}$. We will refer to the combination of all six two-point functions as 6×2pt, and the combination of all two-point functions except for $w^{\kappa_{\rm CMB}\kappa_{\rm CMB}}(\theta)$ as 5×2pt.

In this work, we develop the methodology for jointly analyzing the 5×2pt set of correlation functions. This methodology will be applied to measurements of the 5×2pt two-point functions using data from DES, SPT and *Planck* in a companion paper, extending the 3×2pt analysis of DES Collaboration et al. (2017). We do not include $w^{\kappa_{\rm CMB}\kappa_{\rm CMB}}(\theta)$ in the analysis presented here because the current highest signal-to-noise measurement of $w^{\kappa_{\rm CMB}\kappa_{\rm CMB}}(\theta)$ comes from Planck Collaboration et al. (2016a). Since the *Planck* $\kappa_{\rm CMB}$ map covers the full sky, the covariance between $w^{\kappa_{\rm CMB}\kappa_{\rm CMB}}(\theta)$ measured by *Planck* and set of 5×2pt correlations involving current SPT and DES Y1 data (which overlap over roughly 1300 sq. deg. on the sky) is negligible. Therefore, cosmological constraints from the *Planck* measurement of $w^{\kappa_{\rm CMB}\kappa_{\rm CMB}}(\theta)$ can be trivially combined with those from the 5×2pt analysis by taking the product of the corresponding posteriors. For future DES and SPT data, the improved signal-to-noise of the measurements may necessitate revisiting the approximation of negligible covariance between the *Planck* measurement of $w^{\kappa_{\rm CMB}\kappa_{\rm CMB}}(\theta)$ and the DES and SPT measurements of 5×2pt.

The analysis presented here builds on the methodology presented in Krause et al. (2017) (hereafter K17) for analyzing the 3×2pt data vector. The most significant difference between this work and that of K17 is that we must account for sources of systematic error that are specific to the cross-correlations with $\kappa_{\rm CMB}$. Of these systematics, the most problematic is contamination of $\kappa_{\rm CMB}$ by the thermal Sunyaev-Zel'dovich effect (tSZ). In the context of measurements of the CMB lensing autospectrum, the effect of tSZ (and other potential contaminants) on $\kappa_{\rm CMB}$ has been investigated previously by e.g. van Engelen et al. (2014). We develop an approach for estimating the effects of such contamination on $w^{\delta_g\kappa_{\rm CMB}}(\theta)$ and $w^{\gamma\kappa_{\rm CMB}}(\theta)$, and use these estimates to determine an appropriate choice of angular scale cuts to apply to the two-point function measurements to minimize tSZ-induced bias.

After developing the methodology for analyzing the 5×2pt data vector, we use simulated likelihood analyses to demonstrate how adding the cross-correlations with $\kappa_{\rm CMB}$ to the 3×2pt analysis can improve cosmological constraints and can potentially allow for the self-calibration of nuisance parameters that are degenerate with cosmology in the 3×2pt analysis. While the currently low signal-to-noise of the $w^{\delta_g\kappa_{\rm CMB}}(\theta)$ and $w^{\gamma\kappa_{\rm CMB}}(\theta)$ correlation functions limits their cosmological constraining power, we show that including them in the joint analysis can make the cosmological constraints more robust to multiplicative shear biases.

This work builds on several recent DES collaboration papers that analyze two-point functions of DES observables. These include the analysis of cosmic shear (Troxel et al. 2017), the analysis of galaxy clustering (Elvin-Poole et al. 2017), the analysis of galaxy-galaxy lensing (Prat et al. 2017), and the joint analysis of all three two-point functions in DES Collaboration et al. (2017).

The layout of the paper is as follows. In §2 we describe the datasets used in this work; in §3 we describe the modeling steps required to compute a likelihood for the observed two-point functions given a cosmological model; in §4 we describe our procedure for characterizing systematic biases in $w^{\delta_g\kappa_{\rm CMB}}(\theta)$ and $w^{\gamma\kappa_{\rm CMB}}(\theta)$ that are specific to the $\kappa_{\rm CMB}$ maps; in §5 we describe the motivation for our choice of angular scale cuts. We present results from simulated analyses in §6 and conclude in §7.

2 DATA

This work presents the *methodology* for analyzing the two-point functions formed between δ_g, γ and $\kappa_{\rm CMB}$. For the most part, developing this methodology does not rely on analyzing any actual data. However, in §4, we will take a data-driven approach to characterizing biases in $w^{\delta_g\kappa_{\rm CMB}}(\theta)$ and $w^{\gamma\kappa_{\rm CMB}}(\theta)$ due to contamination of the $\kappa_{\rm CMB}$ maps. For that part of the analysis, we rely on exactly the same galaxy and shear catalogs used in the DES 3×2pt analysis (DES Collaboration et al. 2017). Below, we briefly describe these catalogs and refer readers to the listed references for more details.

---

[1] We will use the notation $w^{XY}(\theta)$ to represent the configuration space, two-point correlation function between fields X and Y. We will use the notation $C^{XY}(\ell)$ to represent the harmonic space cross-power spectrum between two fields.

We consider measurements of $w^{\delta_g \kappa_{\rm CMB}}(\theta)$ and $w^{\gamma \kappa_{\rm CMB}}(\theta)$ in configuration space, i.e. as a function of the angle between the two points being correlated. Measuring $w^{\delta_g \kappa_{\rm CMB}}(\theta)$ and $w^{\gamma \kappa_{\rm CMB}}(\theta)$ requires two sets of galaxies, which we refer to as 'lenses' and 'sources.' Lenses are treated as tracers of the matter density field and are used to measure δ_g; images of the source galaxies are used to measure the gravitational lensing-induced shears, γ. The lens and source galaxies are in turn divided into multiple redshift bins.

2.1 Galaxy catalog

For the purposes of measuring δ_g, we use a subset of the DES Y1 'Gold' catalog (Drlica-Wagner et al. 2017) referred to as redMaGiC (Rozo et al. 2016). The redMaGiC galaxies are a set of luminous red galaxies (LRGs) selected based on their match to a red sequence template, which is calibrated via the redMaPPer galaxy-cluster-finding algorithm (Rykoff et al. 2014; Rozo et al. 2016; Rykoff et al. 2016). The redMaGiC galaxies are designed to have very well understood photometric redshift estimates, with a scatter of $\sigma_z \sim 0.017(1+z)$ (Elvin-Poole et al. 2017). As in K17, the redMaGiC galaxies are divided into 5 redshift bins at $0.15 \lesssim z \lesssim 0.9$, where the three lower redshift bins have a luminosity threshold of $L_{\rm min} = 0.5L^*$ and the two higher redshift bins have luminosity thresholds $L_{\rm min} = 1.0L^*$ and $1.5L^*$, respectively. For a more detailed description of the galaxy sample, see also Prat et al. (2017); Elvin-Poole et al. (2017).

2.2 Shear catalog

For the purposes of measuring γ, we use the same shear catalogs used in the 3×2pt analysis. Two shear measurement algorithms – MetaCalibration (Huff & Mandelbaum 2017; Sheldon & Huff 2017) and Im3shape (Zuntz et al. 2013) – were used to generate the galaxy shear catalogs that were used in the 3×2pt analysis, while the MetaCalibration catalog was used as the fiducial catalog due to its higher signal-to-noise. MetaCalibration uses the data itself to calibrate the bias in shear estimation by artificially shearing the galaxy images and re-measuring the shear. Im3shape, on the other hand, invokes a large number of sophisticated image simulations to calibrate the bias in shear estimates. As in K17, the shear catalogs were divided into four redshift bins between $z \sim 0.2$ and 1.3. For a detailed description of both shear catalogs, see Zuntz et al. (2017). For details of the photo-z catalog associated with the shear catalogs, see Hoyle et al. (2017). The analysis presented in this work adopts noise estimates and redshift distributions corresponding to the MetaCalibration catalog.

2.3 CMB lensing map

The methodology presented here is general and could be applied to any map of $\kappa_{\rm CMB}$. However, in order to accurately characterize the magnitude of biases in $\kappa_{\rm CMB}$, we tailor our analysis to the $\kappa_{\rm CMB}$ maps that will be used in the companion paper that presents cosmological constraints obtained from analysis of the 5×2pt data vector. That work will use the $\kappa_{\rm CMB}$ maps from Omori et al. (2017) (henceforth O17) and so we briefly describe those maps here.

The $\kappa_{\rm CMB}$ map generated in O17 is computed by applying the quadratic lensing estimator of Hu & Okamoto (2002) to an inverse variance weighted combination of 150 GHz SPT and 143 GHz *Planck* temperature maps. The quadratic estimator of Hu & Okamoto (2002) exploits the fact that gravitational lensing induces a correlation between the gradient of the CMB temperature field and small-scale fluctuations in this field. A suitably normalized quadratic combination of filtered CMB temperature maps then provides an estimate of $\kappa_{\rm CMB}$. The SPT maps used for this purpose are from the SPT-SZ survey (Story et al. 2013). The combined map produced from the SPT and *Planck* datasets is sensitive to a greater range of angular modes on the sky than either experiment alone: *Planck* cannot measure small scale modes because of its 7' beam (at 143 GHz), while SPT cannot measure large scale modes because of time domain filtering that is used to remove atmospheric contamination.

The $\kappa_{\rm CMB}$ map from Omori et al. (2017) is restricted to the area of sky that is observed by both SPT and *Planck* . The overlap of this region with the DES Y1 survey region is approximately 1300 sq. deg.

3 MODELING THE TWO-POINT FUNCTIONS

3.1 Formalism

We begin by describing the formalism used to model the 5×2pt set of correlation functions. This methodology closely follows that described in K17 to model the 3×2pt data vector. We consider exactly the same galaxy selections, and make many of the same modeling assumptions. To minimize repetition, in this work, we focus only on describing the modeling of those correlations that involve $\kappa_{\rm CMB}$ (i.e. $w^{\delta_g \kappa_{\rm CMB}}(\theta)$ and $w^{\gamma \kappa_{\rm CMB}}(\theta)$); for a complete description of the modeling of the other two-point functions (i.e. $w^{\delta_g \delta_g}(\theta)$, $w^{\delta_g \gamma}(\theta)$, and $w^{\gamma\gamma}(\theta)$), we refer readers to K17.

When measuring the correlation between DES shears and $\kappa_{\rm CMB}$, we consider only the component of the shear that is oriented orthogonally to the line connecting the two points being correlated, i.e. the tangential shear, $\gamma_{\rm t}$. In the weak shear limit, this tangential component contains all the lensing signal (Bartelmann & Schneider 2001). Using $\gamma_{\rm t}$ has the advantage of reducing contamination from additive systematics in the shear estimation and avoiding mask effects during the conversion from γ to κ (Harnois-Déraps et al. 2016). Henceforth, we will denote this correlation as $w^{\gamma_{\rm t} \kappa_{\rm CMB}}(\theta)$.

We begin by computing the cross-spectra between the relevant fields in harmonic space using the Limber approximation (Limber 1953). For computing $w^{\gamma_{\rm t} \kappa_{\rm CMB}}(\theta)$, it is convenient to first express this cross-correlation in terms of lensing convergence, rather than shear, and then transform to shear when expressing the correlation function in configuration space. The lensing convergence, κ, in some direction specified by $\hat{\theta}$, is defined by

$$\kappa(\hat{\theta}, \chi_s) = \frac{3\Omega_{\rm m} H_0^2}{2c^2} \int_0^{\chi_s} d\chi' \frac{\chi'(\chi - \chi')}{\chi} \frac{\delta(\hat{\theta}, \chi')}{a(\chi')}, \tag{1}$$

where χ is comoving distance (with χ_s being the comoving distance to the source plane), H_0 is the Hubble constant today, $\Omega_{\rm m}$ is the matter density today, δ is the matter overdensity, and a is the scale factor (Bartelmann & Schneider 2001). We refer to the lensing convergence defined for the source galaxies as κ_s (in contrast to the CMB-derived lensing convergence, $\kappa_{\rm CMB}$). For galaxy lensing, the sources are distributed across a broad range of redshift and the convergence must be averaged across this distribution. In this case, the convergence for source galaxies in the ith redshift bin becomes

$$\kappa_s^i(\hat{\theta}) = \int_0^{\infty} d\chi' q^i_{\kappa_s}(\chi') \delta(\hat{\theta}, \chi'), \tag{2}$$

where we have defined the lensing weight as

$$q^i_{\kappa_s}(\chi) = \frac{3\Omega_m H_0^2}{2c^2}\frac{\chi}{a(\chi)}\int_{\chi}^{\infty} d\chi' \frac{n^i_s(z(\chi'))\frac{dz}{d\chi'}}{\bar{n}^i_s}\frac{\chi'-\chi}{\chi'}, \tag{3}$$

where $n_s(z)$ the number density of the source galaxies as a function of redshift, and $\bar{n}^i_s$ is the average of that quantity over redshift. Since the CMB originates from a very narrow range of comoving distance, we can approximate the source redshift distribution of the CMB as a Dirac δ-function centered on the comoving distance to the last scattering surface, χ^*. In this case, the lensing weight function for CMB lensing becomes

$$q_{\kappa_{\rm CMB}}(\chi) = \frac{3\Omega_{\rm m} H_0^2}{2c^2}\frac{\chi}{a(\chi)}\frac{\chi^*-\chi}{\chi^*}. \tag{4}$$

The overdensity of galaxies on the sky in the ith redshift bin can also be related to an integral along the line of sight of the matter overdensity, assuming the galaxy bias is known. Following DES Collaboration et al. (2017), we restrict our analysis to the linear bias regime, where the galaxy overdensity can be expressed as $\delta_g(\hat{\theta},\chi) = b_g(\chi)\delta(\hat{\theta},\chi)$, where $b_g(\chi)$ is the galaxy bias. In this case, the projected overdensity of galaxies on the sky is

$$\delta^i_g(\hat{\theta}) = \int d\chi' q^i_{\delta_g}(\chi')\delta(\hat{\theta},\chi'), \tag{5}$$

where we have defined the lens galaxy weight function as

$$q^i_{\delta_g}(\chi) = b^i_g(\chi)\frac{n^i_g(z(\chi))}{\bar{n}^i_g}\frac{dz}{d\chi}, \tag{6}$$

where $n^i_g(z)$ is the number density of the lens galaxies in the ith bin as a function of redshift. We will further simplify the bias modeling such that the bias for each galaxy redshift bin is assumed to be a constant, b^i_g. In reality, the linear bias model is known to break down at small scales (Zehavi et al. 2005; Blanton et al. 2006; Cresswell & Percival 2009). We will show in §5 that for our choice of angular scale cuts, the assumption of linear bias does not bias our parameter constraints.

Using the Limber approximation, we have

$$C^{\kappa_s\kappa_{\rm CMB}}(\ell) = \int d\chi \frac{q^i_{\kappa_s}(\chi)q_{\kappa_{\rm CMB}}(\chi)}{\chi^2}P_{\rm NL}\left(\frac{\ell+1/2}{\chi}, z(\chi)\right), \tag{7}$$

and

$$C^{\delta_g\kappa_{\rm CMB}}(\ell) = \int d\chi \frac{q^i_{\delta_g}(\chi)\,q_{\kappa_{\rm CMB}}(\chi)}{\chi^2}P_{\rm NL}\left(\frac{\ell+1/2}{\chi}, z(\chi)\right), \tag{8}$$

where i labels the redshift bin (of either the lens or source galaxies) and $P_{\rm NL}(k,z)$ is the nonlinear matter power spectrum. We compute the nonlinear power spectrum using the Boltzmann code CAMB[2] (Lewis et al. 2000; Howlett et al. 2012) with the Halofit extension to nonlinear scales (Smith et al. 2003; Takahashi et al. 2012) and the Bird et al. (2012) neutrino extension.

SPT and *Planck* observe the CMB with finite-size beams. When generating the $\kappa_{\rm CMB}$ map, this beam is deconvolved, exponentially increasing noise at small scales. Unfortunately, the presence of small-scale noise in $\kappa_{\rm CMB}$ will make the real-space covariance diverge. To prevent this divergence, we apply a smoothing function to the $\kappa_{\rm CMB}$ maps. We convolve the maps with a Gaussian beam having full width at half maximum of $\theta_{\rm FWHM} = 5.4'$. In harmonic space, this corresponds to multiplication of the maps by

$$B(\ell) = \exp(-\ell(\ell+1)/\ell^2_{\rm beam}), \tag{9}$$

where $\ell_{\rm beam} \equiv \sqrt{16\ln 2}/\theta_{\rm FWHM} \approx 2120$. Additionally, we filter out modes in the $\kappa_{\rm CMB}$ map with $\ell < 30$ and $\ell > 3000$, where the lower bound is to avoid the potential contamination coming from the mean-field calibration in the $\kappa_{\rm CMB}$ lensing map (Omori et al. 2017) and the upper limit is imposed to remove potential biases due to foregrounds in the $\kappa_{\rm CMB}$ map. The impact of this filtering can be seen in Fig. 1.

Converting the above expressions to configuration-space correlation functions via a Legendre transform yields

$$\begin{aligned} w^{\gamma^i_{\rm t}\kappa_{\rm CMB}}(\theta) &= \int \frac{d\ell\,\ell}{2\pi}F(\ell)J_2(\ell\theta)C^{\kappa_s\kappa_{\rm CMB}}(\ell), & (10)\\ w^{\delta^i_g\kappa_{\rm CMB}}(\theta) &= \sum \frac{2\ell+1}{4\pi}F(\ell)P_\ell(\cos(\theta))C^{\delta^i_g\kappa_{\rm CMB}}(\ell), & (11)\end{aligned}$$

where J_2 is the second order Bessel function of the first kind and P_l is the ℓth order Legendre polynomial. The appearance of J_2 in Eq. 10 is a consequence of our decision to measure the correlation of $\kappa_{\rm CMB}$ with tangential shear. The function $F(\ell) = B(\ell)\Theta(\ell-30)\Theta(3000-\ell)$, where $\Theta(\ell)$ is a step function, describes the filtering that is applied to the $\kappa_{\rm CMB}$ map. Henceforth, for notational convenience, we will suppress the redshift bin labels on the correlation functions. We show the model $w^{\delta_g\kappa_{\rm CMB}}(\theta)$ and $w^{\gamma_t\kappa_{\rm CMB}}(\theta)$ corresponding to the best-fit *Planck* cosmological parameters in Fig. 1.

3.2 Modeling systematics affecting δ_g and γ

There are several sources of systematic uncertainty that affect the δ_g and γ observables. These systematics will propagate into the $w^{\delta_g\kappa_{\rm CMB}}(\theta)$ and $w^{\gamma_t\kappa_{\rm CMB}}(\theta)$ measurements. We model these sources of systematic error exactly as described in K17, and so provide only a brief description here. We will consider sources of systematic error that can affect the $\kappa_{\rm CMB}$ map in more detail in §4.

3.2.1 Shear calibration bias

The inference of γ from an image of a galaxy is subject to sources of systematic error. Such errors are commonly parameterized in terms of a multiplicative bias, m, such that the observed shear is related to the true shear by $\gamma_{\rm obs} = (1+m)\gamma_{\rm true}$ (e.g. Zuntz et al. 2017). While additive biases may also be present in shear calibration, these are typically tightly constrained by the data itself (and are minimized by our decision to use the tangential shear component).

Following K17 and other literature (Abbott et al. 2016; Joudaki et al. 2017; Hildebrandt et al. 2017), we adopt a separate multiplicative bias parameter, m_i, for the ith source galaxy redshift bin. The model for $w^{\gamma_t\kappa_{\rm CMB}}(\theta)$ (Eq. 10) is then scaled by $(1+m_i)$. Note, however, that $w^{\delta_g\kappa_{\rm CMB}}(\theta)$ does not depend on the estimated shears and is therefore unaffected by m_i.

3.2.2 Intrinsic alignment

In addition to the coherent alignment of galaxy shapes caused by gravitational lensing, galaxy shapes can also be intrinsically aligned as a result of e.g. tidal fields (Heavens et al. 2000; Catelan & Porciani 2001; Crittenden et al. 2001). Such *intrinsic alignments* constitute a potential systematic for the measurement of gravitational lensing from galaxy shapes. Intrinsic alignments of galaxies will also affect $w^{\gamma_t\kappa_{\rm CMB}}(\theta)$ (Hall & Taylor 2014; Troxel & Ishak 2014). To see this, consider a galaxy that is stretched by the tidal field of nearby large scale structure; the same large scale structure

---

[2] See `camb.info`.

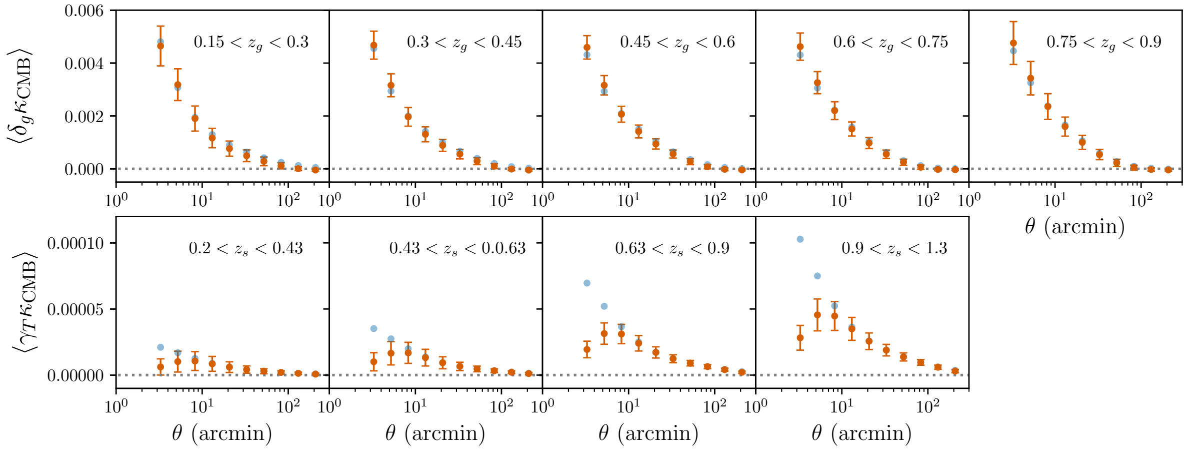

Figure 1. Models of the $w^{\delta_g \kappa_{\rm CMB}}(\theta)$ and $w^{\gamma_t \kappa_{\rm CMB}}(\theta)$ correlation functions corresponding to the fiducial cosmological model of Table 1 (orange points with errorbars). Each panel represents the correlation function for a different lens or source redshift bin. Error bars correspond to the square root of the diagonal elements of the covariance matrix described in §3.3. Blue points show the model vectors in the absence of the harmonic-space filtering of the $\kappa_{\rm CMB}$ map described in §3.1; the filtering affects $w^{\delta_g \kappa_{\rm CMB}}(\theta)$ and $w^{\gamma_t \kappa_{\rm CMB}}(\theta)$ differently because of the non-local nature of γ_t.

that causes this intrinsic alignment will also lens the CMB, leading to a correlation between the intrinsic galaxy shapes and $\kappa_{\rm CMB}$. This effect is analogous to the usual gravitational-intrinsic (GI) term affecting $w^{\gamma\gamma}(\theta)$ (Hirata & Seljak 2004). Following K17, we parameterize the effects of intrinsic alignments using the nonlinear linear alignment (NLA) model (Bridle & King 2007). This model impacts q_κ for the source galaxies as described in K17.

Briefly, we perform the replacement

$$q^i_{\kappa_s}(\chi) \to q^i_{\kappa_s}(\chi) - A(z(\chi)) \frac{n^i_s(z(\chi))}{\bar{n}^i_s} \frac{dz}{d\chi}, \tag{12}$$

where

$$A(z) = A_{\rm IA,0} \left(\frac{1+z}{1+z_0} \right)^{\alpha_{\rm IA}} \frac{0.0139\Omega_m}{D(z)}, \tag{13}$$

where $D(z)$ is the linear growth factor and we set $z_0 = 0.62$. The normalization $A_{\rm IA,0}$ and power law scaling with redshift, $\alpha_{\rm IA}$ are treated as free parameters of the model.

3.2.3 *Photometric redshift errors*

DES uses multiband optical photometry to infer the redshift distributions of the galaxy samples (it is these distributions that are necessary for modeling the 5×2pt set of correlation functions). This inference is potentially subject to sources of systematic error, which can result in biases to $n_g(z)$ and $n_s(z)$. Following K17 and other literature (Abbott et al. 2016; Joudaki et al. 2017; Hildebrandt et al. 2017), we parameterize such biases in terms of the shift parameters, Δ_z, such that the estimated redshift distribution, $\hat{n}(z)$ is related to the true redshift distribution, $n_{\rm true}(z)$, via $n_{\rm true}(z) = \hat{n}(z - \Delta_z)$. We consider separate shift parameters for each lens and source galaxy redshift bin, $\Delta^i_{z,g}$ and $\Delta^i_{z,s}$, respectively, where the i superscript labels the redshift bin.

3.3 Covariance

The DES 3×2pt analysis uses a halo model covariance, as described and validated in K17. We now describe the extension of this formalism to the CMB lensing cross-correlations $w^{\delta_g \kappa_{\rm CMB}}(\theta)$ and $w^{\gamma_t \kappa_{\rm CMB}}(\theta)$. For notational convenience, we will use $\Sigma(\theta)$ and $\Sigma(\ell)$ to generically represent one of these two-point functions in configuration and harmonic space, respectively; we will use $\Xi(\theta)$ and $\Xi(\ell)$ to represent one of the 3×2pt correlation functions (i.e. $w^{\delta_g \delta_g}(\theta)$, $w^{\delta_g \gamma_t}(\theta)$, $\xi_+(\theta)$ and $\xi_-(\theta)$) in configuration and harmonic space, respectively. We calculate the covariance of the harmonic space correlation functions, $\mathrm{Cov}(\Sigma^i(\ell), \Sigma^k(\ell'))$ as the sum of a Gaussian covariance $\mathrm{Cov}^{\rm G}$ and non-Gaussian covariance $\mathrm{Cov}^{\rm NG}$, which includes super-sample variance (Takada & Hu 2013), as detailed in Krause & Eifler (2017) and Schaan et al. (2017), using the halo model to compute the higher-order matter correlation functions. The covariance of the $w^{\delta_g \kappa_{\rm CMB}}(\theta)$ and $w^{\gamma_t \kappa_{\rm CMB}}(\theta)$ is then

$$\mathrm{Cov}\left(\Sigma^i(\theta),\, \Sigma^k(\theta')\right) = \int \frac{d\ell\, \ell}{2\pi} J_{n(\Sigma^i)}(\ell\theta) F(\ell) \int \frac{d\ell'\, \ell'}{2\pi} J_{n(\Sigma^k)}(\ell'\theta') F(\ell') \left[\mathrm{Cov}^{\rm G}\left(\Sigma^i(\ell), \Sigma^k(\ell')\right) + \mathrm{Cov}^{\rm NG}\left(\Sigma^i(\ell), \Sigma^k(\ell')\right)\right], \tag{14}$$

where J_n is the nth-order Bessel function of the first kind, and $F(\ell)$ is the function that describes the filtering that is applied to the $\kappa_{\rm CMB}$ map. The cross-covariance between $w^{\delta_g \kappa_{\rm CMB}}(\theta)$ and $w^{\gamma_t \kappa_{\rm CMB}}(\theta)$ with one of the DES 3×2pt correlation functions is given by

$$\mathrm{Cov}\left(\Sigma^i(\theta),\, \Xi^k(\theta')\right) = \int \frac{d\ell\, \ell}{2\pi} J_{n(\Sigma)}(\ell\theta) \int \frac{d\ell'\, \ell'}{2\pi} J_{n(\Xi)}(\ell'\theta') \left[\mathrm{Cov}^{\rm G}\left(\Sigma^i(\ell), \Xi^k(\ell')\right) + \mathrm{Cov}^{\rm NG}\left(\Sigma^i(\ell), \Xi^k(\ell')\right)\right], \tag{15}$$

where the order of the Bessel function is given by $n = 0$ for $w^{\delta_g \kappa_{\rm CMB}}(\theta)$, $w^{\delta_g \delta_g}(\theta)$, and ξ_+, by $n = 2$ for $w^{\gamma_t \kappa_{\rm CMB}}(\theta)$ and $w^{\delta_g \gamma_t}(\theta)$, and by $n = 4$ for ξ_-.

3.4 Likelihood analysis

We now build the likelihood of the data given the model described in §3.1 and the covariance described in §3.3. The model includes parameters describing cosmology, galaxy bias, intrinsic alignment, and shear and photo-z systematics. The cosmological model considered in this analysis is flat ΛCDM. The cosmological parameters varied are the present day matter density parameter, $\Omega_{\rm m}$, the normalization of the primordial power spectrum, $A_{\rm s}$, the spectral index of the primordial power spectrum, n_s, the present day baryon

Table 1. Parameters of the baseline model: fiducial values, flat priors (min, max), and Gaussian priors (μ, σ). Definitions of the parameters can be found in the text. The cosmological model considered is spatially flat ΛCDM, so the curvature density parameter and equation of state of dark energy are fixed to $\Omega_K = 0$ and $w = -1$, respectively.

Parameter	Fiducial	Prior
	Cosmology	
Ω_m	0.295	flat (0.1, 0.9)
$A_s/10^{-9}$	2.26	flat (0.5,5.0)
n_s	0.968	flat (0.87, 1.07)
w_0	-1.0	fixed
Ω_b	0.0468	flat (0.03, 0.07)
h_0	0.6881	flat (0.55, 0.91)
$\Omega_\nu h^2$	6.16×10^{-4}	fixed
Ω_K	0	fixed
	Galaxy bias	
b_g^1	1.35	flat (0.8, 3.0)
b_g^2	1.55	flat (0.8, 3.0)
b_g^3	1.65	flat (0.8, 3.0)
b_g^4	1.8	flat (0.8, 3.0)
b_g^5	2.0	flat (0.8, 3.0)
	Lens photo-z bias	
$\Delta_{z,g}^1$	0.002	Gauss (0.0, 0.007)
$\Delta_{z,g}^2$	0.001	Gauss (0.0, 0.007)
$\Delta_{z,g}^3$	0.003	Gauss (0.0, 0.006)
$\Delta_{z,g}^4$	0.0	Gauss (0.0, 0.01)
$\Delta_{z,g}^5$	0.0	Gauss (0.0, 0.01)
	Source photo-z bias	
$\Delta_{z,s}^1$	-0.002	Gauss (-0.001,0.016)
$\Delta_{z,s}^2$	-0.0015	Gauss (-0.019,0.013)
$\Delta_{z,s}^3$	0.007	Gauss (0.009, 0.011)
$\Delta_{z,s}^4$	-0.018	Gauss (-0.018, 0.022)
	Shear Calibration bias	
m^i	0.013	Gauss (0.012, 0.023)
	Intrinsic Alignments	
$A_{IA,0}$	0.0	flat (-5.0, 5.0)
α_{IA}	0.0	flat (-5.0, 5.0)
z_0	0.62	fixed

density parameter, Ω_b, and the Hubble parameter today, h_0. The complete set of model parameters is summarized in Table 1. For the simulated likelihood analyses described below, we generate a data vector at a fiducial set of model parameters given by the middle column of Table 1. The priors imposed in our fiducial likelihood analysis are given in the third column of Table 1; these priors are identical to those of the 3×2pt analysis of DES Collaboration et al. (2017).

For the purposes of this analysis, we keep the cosmological density of neutrinos fixed to $\Omega_\nu h^2 = 6.16 \times 10^{-4}$, corresponding to a total neutrino mass of 0.06 eV. This choice is reasonable since the DES Collaboration et al. (2017) analysis only weakly constrains the neutrino mass, and the 5×2pt analysis does not significantly improve on these constraints.

Given a point in parameter space, **p**, we consider a Gaussian likelihood for the 5×2pt observable, **d**:

$$\mathcal{L}(\mathbf{d}|\mathbf{p}) \propto \exp\left[-\frac{1}{2}\sum_{ij}(d_i - m_i(\mathbf{p}))\left[\mathbf{C}^{-1}\right]_{ij}(d_j - m_j(\mathbf{p}))\right], \quad (16)$$

where **m** is the model vector, the sum runs over all elements of the data vector, and **C** is the covariance matrix described in §3.3. As in K17, we keep the covariance matrix fixed as a function of cosmological parameters. This ignores the cosmology-dependence of the covariance matrix (Morrison & Schneider 2013; Eifler et al. 2009), which is negligible compared to the noise level in the DES Y1 and SPT data.

The computation of the model vector and the likelihood analysis is performed in `CosmoSIS` (Zuntz et al. 2015). We sample parameter space using the `multinest` algorithm (Feroz et al. 2009). The `multinest` sampler has been tested in K17 to yield results consistent those of another sampler, `emcee` (Foreman-Mackey et al. 2013), which relies on the algorithm of Goodman & Weare (2010).

4 BIASES IN THE $\kappa_{\rm CMB}$ MAPS

4.1 Overview

While the systematics considered in §3.2 affect both the 3×2pt data vector and the 5×2pt data vector, there are also sources of systematic error that impact only $w^{\delta_g \kappa_{\rm CMB}}(\theta)$ and $w^{\gamma_t \kappa_{\rm CMB}}(\theta)$. In this section, we attempt to quantify biases in the $\kappa_{\rm CMB}$ maps that will affect the measurement of these two correlation functions.

We write the observed $\kappa_{\rm CMB}$ signal on the sky, $\kappa_{\rm obs}$, as the sum of the true CMB lensing signal, $\kappa_{\rm CMB}$, and some contaminating field, $\kappa_{\rm sys}$, i.e. $\kappa_{\rm obs} = \kappa_{\rm CMB} + \kappa_{\rm sys}$. The observed correlation functions $w^{\delta_g \kappa_{\rm obs}}(\theta)$ and $w^{\gamma_t \kappa_{\rm obs}}(\theta)$ then differ from the correlation functions with the true $\kappa_{\rm CMB}$ by $w^{\gamma_t \kappa_{\rm sys}}(\theta)$ and $w^{\delta_g \kappa_{\rm sys}}(\theta)$. To determine these biases, we will form an estimate of $\kappa_{\rm sys}$ and then use the true galaxy and shear catalogs described in §2 to calculate $w^{\gamma_t \kappa_{\rm sys}}(\theta)$ and $w^{\delta_g \kappa_{\rm sys}}(\theta)$. However, given the large uncertainties associated with our estimates of $\kappa_{\rm sys}$, we will not attempt to model or correct for such biases in our analysis. Instead, we will choose angular scale cuts such that biases to the inferred posteriors on the model parameters are below 50% of the statistical errors (see discussion in §5).

The dominant sources of bias that contribute to $\kappa_{\rm sys}$ will depend on the methods and data used to estimate $\kappa_{\rm CMB}$. For instance, a $\kappa_{\rm CMB}$ map created from maps of CMB temperature will be affected by bias due to the tSZ effect, while this is not the case for $\kappa_{\rm CMB}$ maps constructed from maps of CMB polarization. Here we tailor our analysis to those systematics that are expected to be dominant for the cross-correlation of DES galaxies and shears with the $\kappa_{\rm CMB}$ maps generated in O17, since it is these $\kappa_{\rm CMB}$ maps that will be used in the forthcoming 5×2pt results paper.

Both the SPT 150 GHz maps and *Planck* 143 GHz maps used to construct the $\kappa_{\rm CMB}$ maps in O17 receive contributions from sources other than primary CMB. In particular, these maps receive significant contributions from the tSZ effect and from radio and thermal dust emission from distant galaxies. The tSZ effect is caused by inverse Compton scattering of CMB photons with hot electrons. At frequencies near 150 GHz, this results in a decrement in the observed CMB temperature. Unresolved galaxies, which together constitute the cosmic infrared background (CIB), on the other hand, appear as a diffuse background in the observed maps. The tSZ and CIB signals on the sky will propagate through the quadratic estimator into the $\kappa_{\rm CMB}$ maps of O17. Since both non-Gaussian sources of contamination are correlated with the matter density, we also expect $\kappa_{\rm sys}$ to be correlated with the matter density. Consequently, these biases will not average to zero in the $w^{\delta_g \kappa_{\rm CMB}}(\theta)$ and $w^{\gamma_t \kappa_{\rm CMB}}(\theta)$ correlations, and we must carefully quantify their impact on our analysis. Note that contamination from the kinematic Sunyaev-Zel'dovich (kSZ) effect is also expected to be present in the $\kappa_{\rm CMB}$ maps. However, since the kSZ signal has a similar morphology to the tSZ signal, but an amplitude that is a factor of ~ 10 smaller, by ensuring that the tSZ effect does not bias our results, we ensure that the kSZ effect also does not lead to a significant bias.

Our approach to estimating $\kappa_{\rm sys}$ due to both tSZ and CIB is to estimate the contributions to the SPT+*Planck* temperature maps from these signals, and to then pass these estimated temperature maps through the quadratic estimator pipeline of O17. To see that this procedure works, consider the total temperature at some multipole, ℓ, as the sum of the lensed CMB and the contaminating signal: $T_{\rm tot}(\ell) = T_{\rm CMB}(\ell) + T_{\rm sys}(\ell)$. The quadratic estimator for the lensing potential $\phi(\mathbf{L})$ is then $\phi(\mathbf{L}) \propto \langle (T(\ell) + T_{\rm sys}(\ell))(T(\ell') + T_{\rm sys}(\ell')) \rangle$, where $\mathbf{L} = \ell + \ell'$. Under the gradient approximation, $T(\ell) \approx \tilde{T}(\ell) + (\nabla \tilde{T} \cdot \nabla \phi)(\ell)$, where the tilde denotes the unlensed field. In the case of both tSZ and CIB bias, terms of the form $T(\ell) T_{\rm sys}(\ell')$ average to zero because the unlensed gradient field is uncorrelated with these biases. Therefore, we have $\phi(\mathbf{L}) \propto \phi(\mathbf{L}) + \phi_{\rm sys}(\mathbf{L})$, where $\phi_{\rm sys}(\mathbf{L})$ is the "lensing" potential associated with the contaminating temperature field.

As we will see below, biases in $w^{\delta_g \kappa_{\rm CMB}}(\theta)$ and $w^{\gamma_t \kappa_{\rm CMB}}(\theta)$ due to the tSZ effect can be quite large, and dominate over all other biases considered. Since massive galaxy clusters are the largest contributors to the tSZ effect on the sky, the level of tSZ bias in the $\kappa_{\rm CMB}$ maps can be reduced by masking these objects. Indeed, O17 masked clusters detected in the SPT maps at high significance via their tSZ decrement before applying the quadratic estimator to the SPT+*Planck* temperature maps. Although masking regions of high tSZ signal reduces the tSZ-induced bias, it has the undesirable consequence of inducing *another* bias in the correlation functions, since the regions of high tSZ signal are also regions of high $\kappa_{\rm CMB}$. We will argue below that this bias is negligible given our masking choices.

We emphasize that the approach taken in this section to characterizing biases in the $\kappa_{\rm CMB}$ map is quite general, and could be applied to characterize biases present in maps other than that of O17. However, the values of the biases obtained here (in particular the measurement of bias due to tSZ contamination) apply only to the $\kappa_{\rm CMB}$ maps of Omori et al. (2017). Maps of $\kappa_{\rm CMB}$ generated from other data sets or using different techniques could have significantly different levels of bias.

4.2 Estimate of bias due to the tSZ effect

4.2.1 Construction of simulated y map

As described above, we estimate tSZ-induced bias in $w^{\delta_g \kappa_{\rm CMB}}(\theta)$ and $w^{\gamma_t \kappa_{\rm CMB}}(\theta)$ by correlating the true galaxy and shear catalogs with an estimate of the bias in the $\kappa_{\rm CMB}$ map due to tSZ signal, which we refer to as $\kappa_{\rm tSZ}$. We estimate $\kappa_{\rm tSZ}$ by applying the quadratic lensing estimator to an estimated map of the tSZ temperature signal in the SPT+*Planck* sky maps. In principle, the tSZ temperature signal could be computed directly from the multi-frequency SPT and *Planck* sky maps. Instead, we take the approach of constructing a *simulated* map of the tSZ signal by placing mock tSZ profiles at the locations of massive galaxy clusters on the sky. One advantage of using a simulated tSZ map instead of generating one from SPT or *Planck* temperature maps is that the simulated map will not be affected by noise in the temperature maps, making it possible to characterize the bias with high statistical accuracy. On the other hand, this approach carries some associated modeling uncertainty, which we will attempt to constrain below.

The cluster sample used to generate the simulated tSZ map combines the redMaPPer (Rykoff et al. 2014) cluster catalog from DES Y1 data with samples of tSZ-detected clusters from SPT and *Planck*. We use redMaPPer clusters with richness $\lambda > 20$, SPT clusters with detection significance $\xi > 4.5$ (Bleem et al. 2015) and the entire *Planck* tSZ-detected cluster sample (Planck Collaboration et al. 2016d). Each of these samples probes a different range of mass and redshift. The redMaPPer sample captures low mass clusters, but only over the redshift range of DES. The SPT cluster sample captures only very massive clusters, but out to high redshift. The *Planck* cluster sample, on the other hand, captures very massive clusters at low redshift which are missed by both SPT and DES.

Of course, there are halos in the Universe that are not detected by redMaPPer, SPT or *Planck* , but nonetheless contribute to the tSZ signal on the sky. However, halos outside of the DES survey region or at redshifts beyond those probed by DES, will not correlate with DES galaxies and shears, and will therefore not bias the inferred correlation functions (although this tSZ contribution will contribute as noise to the measurements). There are also halos within the DES survey region and redshift range that are not detected by any of these three surveys because their corresponding observables are below the detection limit. The lowest mass halos in our sample come from the redMaPPer catalog. The limiting richness threshold of the redMaPPer catalog that we employ is $\lambda = 20$, corresponding roughly to a mass of $M \sim 1.5 \times 10^{14}\, M_\odot$ assuming the mass-richness relation of Melchior et al. (2017). Using simulations, Battaglia et al. (2012) found that halos with masses $M < 2 \times 10^{14}\, M_\odot$ contribute half the tSZ power at $\ell = 3000$, with that fraction decreasing towards lower ℓ. Consequently, for $\ell < 3000$ (the range used to construct the $\kappa_{\rm CMB}$ maps from O17), we expect our simulated map to capture the majority of the tSZ power on the sky. There may also be tSZ signal on the sky that is not due to gas in massive halos, i.e. tSZ signal due to diffuse gas. However, again, this contribution is expected to be subdominant to the contribution of the massive halos and would therefore not significantly change the estimated bias in $\kappa_{\rm CMB}$.

To assign tSZ profiles to the redMaPPer and *Planck* clusters, we first estimate their masses, and then use a model to compute expected tSZ profiles given the estimated masses. For the redMaPPer clusters, the masses are assigned using the mean mass-richness relation of Melchior et al. (2017). For the *Planck* clusters, the masses are assigned using the estimates constructed by Planck Collaboration et al. (2016d) from the observed cluster tSZ signals. In our fiducial analysis we set the hydrostatic bias parameter to $1 - b = 1$ when computing the masses of the *Planck* clusters. Given the mass estimates for the redMaPPer and *Planck* clusters, we compute corresponding pressure profiles using the fits from Battaglia et al. (2012). In particular, the thermal pressure profile is written as

$$P_{\rm th}(x) = P_{200} P_0 (x/x_c)^\gamma \left[1 + (x/x_c)^\alpha\right]^{-\beta}, \tag{17}$$

where $x = r/R_{200c}$ and R_{200c} is the radius from the cluster at which the enclosed mass is M_{200c} and the corresponding mean density is $3M_{200c}/(4\pi R_{200c}^3) = 200\rho_{\rm crit}(z)$. The normalization, P_{200} is given by

$$P_{200} = 200 \frac{G M_{200c} \rho_{\rm crit}(z) f_b}{2 R_{200c}}, \tag{18}$$

where $f_b = \Omega_b/\Omega_m$. The parameters P_0, x_c, α, β, and γ in Eq. 17

are related to the cluster mass, M_{200c}, and redshift as described in Battaglia et al. (2012). The pressure profile is then converted to a Compton-y profile by integrating along the line of sight,

$$y(\theta, M_{200c}, z) = \frac{\sigma_T}{m_e c^2} \int dl\, P_e(\sqrt{l^2 + d_A^2\theta^2}, M_{200c}, z), \tag{19}$$

where σ_T is the Thomson cross-section, m_e is the electron mass, and the term in the integral is the electron pressure (l is the line of sight distance, d_A is the angular diameter distance and θ is the angular separation relative to the cluster center). We assume that the electron pressure, P_e, is given by $P_e = 0.518 P_{\rm th}$. This relation holds when the hydrogen and helium are fully ionized, and the helium mass fraction is $Y = 0.24$.

Finally, the tSZ temperature signal at frequency ν is related to y via

$$\frac{\Delta T(\nu)}{T_{\rm CMB}} = g\left(\frac{h\nu}{k_B T_{\rm CMB}}\right) y, \tag{20}$$

where $g(x) = x(e^x + 1)/(e^x - 1) - 4$ in the limit that the gas is non-relativistic (e.g. Carlstrom et al. 2002).

In contrast to the *Planck* and DES-detected clusters, for the SPT clusters we have a direct measurement of their tSZ profiles, and so use these measurements rather than modeling the profile through an estimate of the cluster masses. Bleem et al. (2015) performed fits to the observed y profiles using the isothermal β model (Cavaliere & Fusco-Femiano 1976), with $\beta = 1$:

$$\Delta T(\theta) = \Delta T_0 (1 + \theta/\theta_c)^{-1}, \tag{21}$$

where θ is the angular distance to the cluster and ΔT_0 and θ_c are parameters of the fit. For the SPT-detected clusters, we use these β-profile fits to estimate their contribution to the y signal on the sky. For any SPT-detected cluster that is also detected by *Planck* or redMaPPer, we use the SPT measurement of its tSZ profile.

As a test of our simulated tSZ map, the left panel of Fig. 2 shows a comparison of the estimated tSZ temperature profiles around the SPT, redMaPPer and *Planck* clusters used to generate the tSZ map. For those SPT-detected clusters that are also detected in the redMaPPer and *Planck* catalogs, we plot the amplitude of the β-profile fits at one arcminute from the cluster center against the corresponding amplitudes of the estimated profiles from Eq. 17. We choose to evaluate the profiles at one arcminute because this is roughly the beam scale of the SPT, so we do not expect the β-profiles to be well constrained below this scale. The left panel of Fig. 2 makes it clear that the estimated tSZ temperature profiles from Eq. 17 agree well with the direct β-profile fits to the observed tSZ signals of the clusters. This agreement is non-trivial: it provides a test of both of the profile model for the simulated tSZ map as well as the mass estimates for both the redMaPPer and *Planck* clusters.

As another check on the model y-profiles, we integrate the simulated profiles for the redMaPPer clusters out to R_{500c} to obtain Y_{500}, and compare these values to the direct measurement of Y_{500} around redMaPPer clusters from Saro et al. (2017). Saro et al. (2017) used a matched filter approach to estimate Y_{500} for redMaPPer clusters detected in DES Science Verification data. We find no evidence for a bias between the simulated and directly estimated Y_{500} for richness $\lambda \gtrsim 60$. At richness $\lambda \lesssim 60$, we find that our model tends to yield higher Y_{500} values, meaning that our model may be somewhat overestimating the effects of tSZ contamination. Note that a similar discrepancy between the measured and predicted profiles was also found by Saro et al. (2017). In that work, it was found that the measured Y_{500} values for clusters with $\lambda < 80$ were smaller than predicted based on assumed scaling relations from Arnaud et al. (2010).

As a further test of our simulated tSZ map, we compute the power spectrum of the map and compare the result to measurements of the y power spectrum from George et al. (2015) and Planck Collaboration et al. (2016b). This comparison is shown in the right panel of Fig. 2. At $\ell = 3000$, our model yields a tSZ power spectrum that is in excellent agreement with that measured by George et al. (2015). At $\ell \gtrsim 3000$, we expect the y signal on the sky to receive significant contributions from low mass ($M \lesssim 2 \times 10^{14}\, M_\odot$) and high redshift halos ($z \gtrsim 0.6$) halos. The fact that our simulated tSZ map does not include low-mass, high-redshift halos yet has power at $\ell = 3000$ that is as large as the George et al. (2015) measurement suggests we may have somewhat overestimated the contribution to the y-signal from the redMaPPer clusters. This explanation is consistent with the finding that our model predicts larger Y_{500} values than measured by Saro et al. (2017) for low richness clusters.

For $\ell \lesssim 1000$, the tSZ power spectrum receives a significant contribution from clusters that are detected by *Planck*, and not by SPT or DES, i.e. high-mass, very low redshift clusters. This can be seen from the fact that when we vary the hydrostatic mass bias parameter used to calculate masses for the *Planck* clusters, the amplitude of the tSZ power spectrum at low ℓ changes significantly. For our fiducial choice of $1 - b = 1.0$, we somewhat underpredict the tSZ power at low ℓ; for $1 - b = 0.6$, we somewhat overpredict the tSZ power at low ℓ, since this effectively assigns the *Planck* clusters larger masses, and thus larger tSZ signals. Although Planck Collaboration et al. (2016c) find evidence for $1 - b = 0.6$, this choice is not well motivated here since we are attempting to invert the SZ-derived masses to obtain an estimate of the corresponding SZ profiles. Consequently, we keep $1 - b = 1.0$ as the fiducial choice for the estimated tSZ map. Note, though, that the amplitude of the inferred bias in $w^{\delta_g \kappa_{\rm CMB}}(\theta)$ and $w^{\gamma_t \kappa_{\rm CMB}}(\theta)$ is almost completely insensitive to the value of $1 - b$ that is assumed because the clusters that are only detected by *Planck* are at very low redshift, and hence do not have strong correlations with DES galaxies or shears.

4.2.2 *Masking clusters to reduce tSZ-induced bias*

Since galaxy clusters are sources of large tSZ signals, tSZ contamination of the $\kappa_{\rm CMB}$ maps can be reduced by masking these objects. O17 masked clusters detected by SPT with signal-to-noise $\xi > 6$ when applying the quadratic lensing estimator to the SPT+*Planck* CMB temperature maps. Applying a more aggressive mask prior to the application of the quadratic estimator is problematic because a complicated mask will lead to difficulties with mode coupling.

In tests on the simulated y-map, we find that tSZ bias of the $\kappa_{\rm CMB}$ map can be further suppressed by masking additional clusters *after* the $\kappa_{\rm CMB}$ reconstruction. This approach works because the application of the quadratic estimator with the filters defined in O17 to a localized tSZ source results in a somewhat-localized κ_{tSZ} signal. Masking clusters post-κ reconstruction, then, can be used to reduce high-ℓ bias in the $\kappa_{\rm CMB}$ maps.

Ultimately, the choice of clusters used for masking is set by the two competing desires to (a) reduce bias in $w^{\delta_g \kappa_{\rm CMB}}(\theta)$ and $w^{\gamma_t \kappa_{\rm CMB}}(\theta)$ due to tSZ, while (b) ensuring that the bias induced by masking regions of high $\kappa_{\rm CMB}$ remains very small (see §4.4 for more discussion of this bias). In tests on the simulated y-maps, we find that masking SPT-detected clusters with $\xi > 5$ and redMaPPer-detected clusters with $\lambda > 80$ post-κ reconstruction can reduce the impact of tSZ bias while inducing an acceptable level of bias due to masking. For all masked clusters, the mask radius employed is 5 ar-

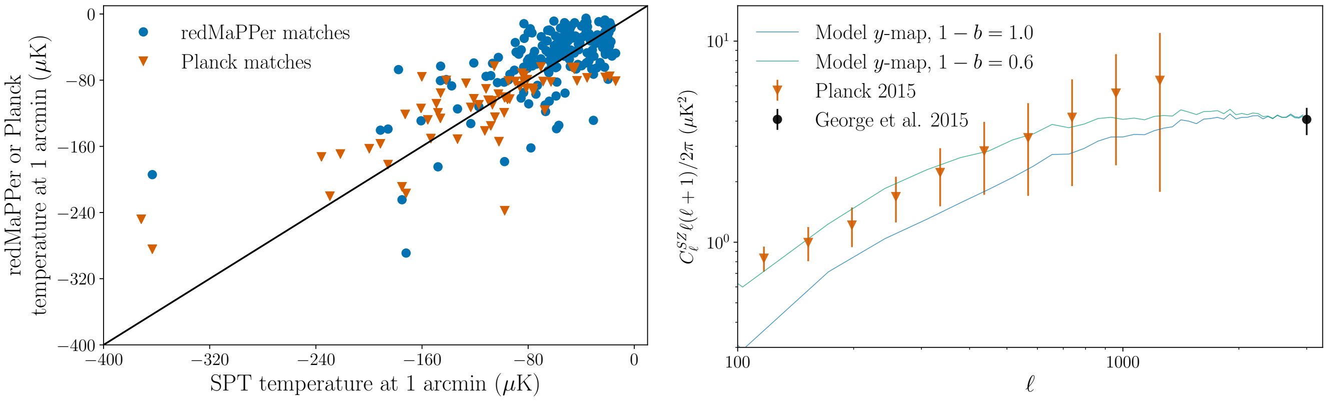

Figure 2. The two panels show different tests of the simulated tSZ map used to estimate the effects of tSZ bias in the $\kappa_{\rm CMB}$ map of O17. The simulated map is generated by placing mock tSZ profiles at the locations of galaxy clusters detected by DES, SPT and *Planck* . (Left) Comparison of the amplitudes of the mock tSZ profiles of clusters detected in the different catalogs. The x-axis represents the tSZ decrement at 150 GHz computed using the β-profile fits of Bleem et al. (2015) to SPT-detected clusters, evaluated at one arcminute from the cluster center. y-axis represents the same quantity computed for redMaPPer (blue circles) and *Planck* -detected (red triangles) clusters using the Battaglia et al. (2012) profile model described in the text. The direct y-profile measurements from Bleem et al. (2015) agree well with the estimated profiles for those clusters that appear in both the SPT catalog and the redMaPPer and *Planck* catalogs. (Right) Power spectrum of the simulated tSZ map compared to measurements from George et al. (2015) and Planck Collaboration et al. (2016b). The two solid lines represent different assumptions about the masses of clusters that are detected by *Planck* and not by SPT or DES. As described in the text, the fiducial analysis assumes the $1-b=1.0$ model, but we find that the estimated bias is insensitive to this assumption. This is not surprising, since the clusters that are only detected by *Planck* live outside of the survey volume of DES, and the resultant bias is therefore largely uncorrelated with the DES galaxies and shears. Errorbars on the *Planck* measurements include both statistical and foreground uncertainties (Planck Collaboration et al. 2016b). The plot is restricted to modes with $100<\ell<3000$ since modes outside this range are not used in the $\kappa_{\rm CMB}$ reconstruction.

cminutes. This choice of masking radius was found to significantly suppress the high ℓ bias from the tSZ in tests on simulations, while simultaneously preserving most of the sky area. The $\xi>5$ masking threshold corresponds roughly to removing clusters with mass $M_{200m}\gtrsim 4\times10^{14}M_\odot$ (Bleem et al. 2015). The $\lambda>80$ threshold corresponds roughly to removing clusters with $M_{200m}\gtrsim 7\times10^{14}M_\odot$ assuming the λ–M relation from Melchior et al. (2017). The fraction of sky area covered by the cluster mask is less than 1%.

4.2.3 *Calculation of bias due to tSZ*

To estimate $\kappa_{\rm tSZ}$, we pass the simulated tSZ temperature map through the $\kappa_{\rm CMB}$ estimation pipeline of Omori et al. (2017). We then correlate $\kappa_{\rm tSZ}$ with the redMaGiC and shear catalogs described in §2.1 and §2.2 to estimate the biases in $w^{\gamma_t\kappa_{\rm CMB}}(\theta)$ and $w^{\delta_g\kappa_{\rm CMB}}(\theta)$.

We measure $C^{\delta_g\kappa_{\rm tSZ}}(\ell)$ and $C^{\kappa_s\kappa_{\rm tSZ}}(\ell)$ in harmonic space using `PolSpice`[3]. Fig. 3 shows these bias functions relative to the theoretical expectation for $C^{\delta_g\kappa_{\rm CMB}}(\ell)$ and $C^{\kappa_s\kappa_{\rm CMB}}(\ell)$ assuming the fiducial cosmological model shown in Table 1. Although the exact values of the estimated biases are cosmology dependent, we are only attempting to determine the scales over which the tSZ bias is significant. The change in these scales is negligible over the range of cosmological models allowed by the data. The tSZ bias is well described by a multiplicative factor that is a smooth function of multipole, and which exhibits mild redshift dependence. The bias in $C^{\delta_g\kappa_{\rm CMB}}(\ell)$ is negative at scales of $\ell\lesssim 2000$, and positive for $\ell\gtrsim 2000$. The amplitudes of these biases can be quite large, reaching a maximum of roughly 25% for $\ell<2000$, and even higher for $\ell>2000$. The tSZ bias in $C^{\kappa_s\kappa_{\rm CMB}}(\ell)$ does not exhibit as strong a peak at small scales as $C^{\delta_g\kappa_{\rm CMB}}(\ell)$, but reaches similar levels of magnitude below $\ell\lesssim 2000$.

Since the redMaPPer catalog is complete to only $z\sim0.7$, we expect our estimate of the tSZ- induced bias in the last two redshift bins of $C^{\delta_g\kappa_{\rm CMB}}(\ell)$ and $C^{\kappa_s\kappa_{\rm CMB}}(\ell)$ to be incomplete, since these bins receive contributions from structure at $z\gtrsim0.7$. We therefore apply our bias measurements for the third-to-last redshift bin to the higher redshift bins. We expect this approximation to be conservative, since the tSZ bias apparently decreases as a function of increasing redshift, as seen in Fig. 3. This decrease is apparently physical, since the completeness of the redMaPPer and SPT catalogs does not evolve significantly over the redshift range $0.15<z<0.6$.

We fit the measured biases with smooth functions to make incorporation into our simulated analyses easier. For the ratio of $C^{\kappa_{\rm tSZ}\delta_g}(\ell)/C^{\kappa_{\rm CMB}\delta_g}_{\rm fid}(\ell)$, we find that the functions defined below provide a good fit:

$$y(\ell)=a(|(\ell-b)/c|)^p\times10^{-8}+d, \tag{22}$$

where a, b, c, d, and p are free parameters for each redshift bin. Similarly, for $C^{\kappa_{\rm tSZ}\kappa_s}(\ell)/C^{\kappa_{\rm CMB}\kappa_s}_{\rm fid}(\ell)$, we use a function of the form:

$$y(\ell)=-a\exp(-(\ell/b))^{1.2}\times10^{-4}+c. \tag{23}$$

The results of these fits are shown as the solid curves in Fig. 3. Given these parameterized fits, we can transform the biases measured in multipole space into biases in angular space (where $w^{\delta_g\kappa_{\rm CMB}}(\theta)$ and $w^{\gamma_t\kappa_{\rm CMB}}(\theta)$ are measured).

Clearly, the biases due to tSZ leakage into $\kappa_{\rm CMB}$ are significant. In §5 we will assess the impact of these biases on the inferred cosmological constraints, and will choose scale cuts to mitigate their impact.

---

[3] `http://www2.iap.fr/users/hivon/software/PolSpice/`

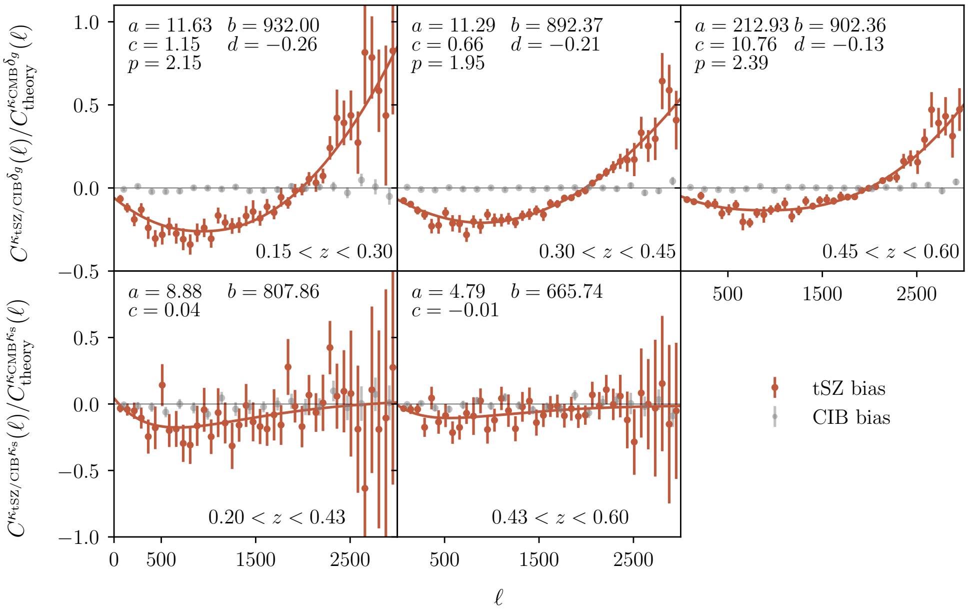

Figure 3. The ratio of the δ_g and γ cross-correlations with the $\kappa_{\rm tSZ}$ map to the theoretical expectation for these correlations with the true $\kappa_{\rm CMB}$ map (prior to applying a Gaussian smoothing of FWHM=5.4'). These measurements form our estimate of the fractional bias in $w^{\delta_g\kappa_{\rm CMB}}(\theta)$ and $w^{\gamma_t\kappa_{\rm CMB}}(\theta)$ due to tSZ contamination of the $\kappa_{\rm CMB}$ map from Omori et al. (2017). Solid curves show model fits to Eqs. 22 and 23, with the best-fit model parameters listed in each panel. Grey points show equivalent quantities for the $\kappa_{\rm CIB}$ map. The error bars shown are calculated using a spatial jackknife method.

4.3 Estimate of CIB bias

To estimate the effects of CIB contamination of the $\kappa_{\rm CMB}$ maps on $w^{\delta_g\kappa_{\rm CMB}}(\theta)$ and $w^{\gamma_t\kappa_{\rm CMB}}(\theta)$, we follow a procedure similar to that used to estimate the tSZ bias. However, rather than generating a simulated CIB map, we instead rely on *Planck* observations. To this end, we use the *Planck* GNILC 545 GHz CIB map (Planck Collaboration et al. 2016e) as a proxy for the true CIB emission on the sky. We first calculate the ℓ-dependent cross-correlation between the combined SPT+*Planck* map and the *Planck* GNILC 545 GHz maps; this correlation provides an estimate of the amount of CIB contamination in the SPT+*Planck* map. The GNILC 545 GHz map is then convolved with the ℓ dependent scaling function:

$$\eta(\ell) = \frac{C_\ell^{\rm GNILC\times SP}}{C_\ell^{\rm GNILC\times GNILC}}, \tag{24}$$

where SP refers to the SPT+*Planck* map. The result is a map of the estimated CIB leakage into the SPT+*Planck* temperature map.

Next, the quadratic estimator is applied to the estimated CIB leakage map to produce $\kappa_{\rm CIB}$, an estimate of the leakage of CIB into the $\kappa_{\rm CMB}$ map. As with $\kappa_{\rm tSZ}$, we cross-correlate $\kappa_{\rm CIB}$ with the true DES galaxy and shear catalogs to form estimates of the bias in $w^{\gamma_t\kappa_{\rm CMB}}(\theta)$ and $w^{\delta_g\kappa_{\rm CMB}}(\theta)$ due to CIB leakage. These cross-correlations are shown in Fig. 3. From the figure, it is apparent our estimate of the CIB bias is consistent with there being no bias, and we will henceforth ignore CIB as a potential source of contamination in our analysis.

4.4 Biases due to masking clusters

As mentioned in §4.2.2, massive galaxy clusters are masked to reduce contamination of $\kappa_{\rm CMB}$ by tSZ leakage. However, clusters are also associated with regions of high $\kappa_{\rm CMB}$. Consequently, by masking these objects, we expect to reduce the amplitude of $w^{\gamma_t\kappa_{\rm CMB}}(\theta)$ and $w^{\delta_g\kappa_{\rm CMB}}(\theta)$ somewhat, which could result in a bias to parameter constraints. Note, though, that the total masked area is quite small because there are relatively few clusters on the sky. Less than 1% of the pre-masking survey area is removed by the cluster mask, which masks 437 clusters.

To characterize masking-induced bias, we generate a simulated $\kappa_{\rm CMB}$ map that consists only of mock cluster $\kappa_{\rm CMB}$ profiles at the locations of the masked clusters in the data; we refer to this map as $\kappa_{\rm sim}$. Each cluster is modeled with an Navarro-Frenk-White (NFW) profile (Navarro et al. 1996). Taking a somewhat simplistic approach, we assign each simulated cluster a mass of $10^{15}\,M_\odot$, which we expect to overestimate the effects of the masking, since most of the masked clusters will have masses less than this. The simulated $\kappa_{\rm sim}$ map is then correlated with the true galaxy and shear catalogs to estimate $w^{\delta_g\kappa_{\rm sim}}(\theta)$ and $w^{\gamma_t\kappa_{\rm sim}}(\theta)$.[4] These two correlation functions effectively represent the parts of $w^{\delta_g\kappa_{\rm CMB}}(\theta)$ and $w^{\gamma_t\kappa_{\rm CMB}}(\theta)$ that we have "missed" by masking the massive galaxy clusters. We find that the ratios of $w^{\gamma_t\kappa_{\rm sim}}(\theta)$ and $w^{\delta_g\kappa_{\rm sim}}(\theta)$ to the true correlation functions are approximately constant with angular scale, and have an average amplitude of approximately 1%. A 1% bias is significantly below the bias induced by e.g. tSZ, and we will therefore ignore it in the subsequent analysis. The level of bias induced by masking is schematically illustrated by the dashed line in Fig. 4.

---

[4] In practice, masked pixels are excluded from the analysis when computing correlation functions. Our estimate of the masking bias, however, corresponds instead to setting these pixels to zero. Given the small angular size of the masked clusters, the difference between these two approaches should be small. If anything, we *overestimate* the effects of masking by computing the bias in this manner.

5 CHOICE OF ANGULAR SCALE CUTS

When modeling the 5×2pt data vector, we neglect nonlinear galaxy bias, the impact of baryons on the matter power spectrum, and the presence of tSZ contamination in the $\kappa_{\rm CMB}$ maps. To prevent these unmodeled effects from causing biases in our cosmological constraints, we restrict our analysis to scales over which their impact is small. In general, these effects become significant at small scales, so this restriction is tantamount to removing small scales from the analysis.

We follow the same basic approach for determining the scale cuts as in K17: we introduce estimates of the unmodeled effects into a simulated data vector generated at the fiducial parameter values from Table 1, and analyze this data vector with varying scale cuts to determine how the parameter constraints are impacted. If the impact of these effects is sufficiently small, we consider our choice of scale cuts sufficient. Our heuristic threshold for an acceptable bias is that the bias on any parameter should not be larger than 50% of the statistical uncertainty on that parameter. The resultant scale cuts reduce the bias in the cosmological constraints to acceptable levels, but at the cost of increasing our statistical errorbars. Future work will be devoted to improving modeling of nonlinear bias, baryons and tSZ bias in order to exploit the additional statistical power in the data.

For the 3×2pt subset of observables, we adopt the same scale cuts as in K17. In principle, the improved signal-to-noise from including $w^{\delta_g\kappa_{\rm CMB}}(\theta)$ and $w^{\gamma_t\kappa_{\rm CMB}}(\theta)$ in the analysis could necessitate more conservative scale cuts for the 3×2pt subset. However, we find below that this is not necessary.

To determine scale cuts for the $w^{\delta_g\kappa_{\rm CMB}}(\theta)$ and $w^{\gamma_t\kappa_{\rm CMB}}(\theta)$ correlation functions, we consider the impact of three systematics that are expected to dominate: tSZ bias in the $\kappa_{\rm CMB}$ maps, nonlinear galaxy bias, and the effects of baryons. Of these, we find that tSZ bias in $\kappa_{\rm CMB}$ is generally dominant. We introduce these effects into the simulated data vectors in the following fashion:

- *tSZ bias:* tSZ bias is introduced into the simulated data vector using the harmonic space fits described in §4 and shown in Fig. 3.

- *Nonlinear galaxy bias:* following K17, we compute the corrections to $w^{\delta_g\kappa_{\rm CMB}}(\theta)$ resulting from the next to leading order bias correction, b_2, and tidal bias term, b_s (McDonald & Roy 2009; Baldauf et al. 2012). These terms are computed using FAST-PT (McEwen et al. 2016).

- *Baryons:* following K17, we introduce baryonic effects into the simulated data vector using results from the OWLS simulations (Schaye et al. 2010). In particular, we use the OWLS AGN model, which is expected to provide an upper limit to the effects of baryons on the matter power spectrum. The modifications to the power spectrum due to baryons are propagated into the mock data vectors using Eqs. 7 and 8.

A potential source of systematic bias considered by K17 was the impact of a one-halo term on $w^{\delta_g\gamma_t}(\theta)$. Since $w^{\delta_g\gamma_t}(\theta)$ mixes power from small scales into large scales, the one-halo term can impact $w^{\delta_g\gamma_t}(\theta)$ at scales significantly beyond the halo virial radius. In contrast, $w^{\delta_g\kappa_{\rm CMB}}(\theta)$ at a projected distance R from halos depends only on the matter power at scales larger than R. Since we exclude small scales of $w^{\delta_g\kappa_{\rm CMB}}(\theta)$ anyway, it is safe to ignore the effects of the one-halo term on $w^{\delta_g\kappa_{\rm CMB}}(\theta)$ in this analysis.

Fig. 4 shows the fractional changes in $w^{\delta_g\kappa_{\rm CMB}}(\theta)$ and $w^{\gamma_t\kappa_{\rm CMB}}(\theta)$ induced by tSZ bias, nonlinear galaxy bias, and the OWLS baryon model. For $w^{\delta_g\kappa_{\rm CMB}}(\theta)$, we plot the fractional change as a function of the projected physical separation evaluated at the mean redshift of the lens galaxies. For $w^{\gamma_t\kappa_{\rm CMB}}(\theta)$, we plot the fractional change as a function of the projected physical separation evaluated at the peak of the lensing kernel of the source galaxies. The errorbars plotted in Fig. 4 are intended to allow comparison between the bias and the statistical uncertainties of the measurements; for better visualization, the errorbars correspond to only 10% of the square root of the diagonal of the covariance matrix. For each angular bin, the bias is not highly significant, but the combined effect from all bins is significant, as we show below.

Fig. 4 also makes it clear that over most scales, tSZ contamination is the most significant source of bias in our analysis. Note that baryons have a fairly small impact on $w^{\delta_g\kappa_{\rm CMB}}(\theta)$, and the nonlinear bias does not impact $w^{\gamma_t\kappa_{\rm CMB}}(\theta)$ at all since this correlation function does not involve biased tracers of the mass. Below scales of about 3 Mpc, bias due to the impact of baryons begins to dominate over the tSZ-induced bias in $w^{\gamma_t\kappa_{\rm CMB}}(\theta)$. Clearly, though, removing tSZ bias from the $\kappa_{\rm CMB}$ maps would allow us to push the analysis to significantly smaller scales.

Our scale cut choice is also illustrated in Fig. 4. The faded points in the figure illustrate the scales that are removed from the analysis by the scale cuts. We exclude angular scales below $(15', 25', 25', 15', 15')$ for the five redshift bins of $w^{\delta_g\kappa_{\rm CMB}}(\theta)$, and below $(40', 40', 60', 60')$ for the four redshift bins of $w^{\gamma_t\kappa_{\rm CMB}}(\theta)$. For $w^{\delta_g\kappa_{\rm CMB}}(\theta)$, the cuts correspond roughly to restricting to scales $R > 8$ Mpc, and somewhat smaller for the lowest redshift bin.

We define the $\Delta\chi^2$ between the biased and unbiased data vectors as

$$\Delta\chi^2 = (\mathbf{d}_{\rm bias} - \mathbf{d}_{\rm fid})^T\, \mathbf{C}^{-1}\, (\mathbf{d}_{\rm bias} - \mathbf{d}_{\rm fid}), \tag{25}$$

where $\mathbf{d}_{\rm bias}$ and $\mathbf{d}_{\rm fid}$ are the data vectors with and without the unmodelled effects, respectively. Including all three unmodeled effects simultaneously, before the application of scale cuts, we find that for the combination of $w^{\delta_g\kappa_{\rm CMB}}(\theta)$ and $w^{\gamma_t\kappa_{\rm CMB}}(\theta)$, $\Delta\chi^2 = 9.7$ (with $\nu = 90$ degrees of freedom). After the scale cuts are imposed, $\Delta\chi^2$ for the $w^{\delta_g\kappa_{\rm CMB}}(\theta)$ and $w^{\gamma_t\kappa_{\rm CMB}}(\theta)$ combination is reduced to only 0.45 (with $\nu = 43$ degrees of freedom). We compute the effect of the residual $\Delta\chi^2$ on the parameter constraints below.

Using the MCMC methods described in §3.4, we compute the posteriors on the full set of model parameters with and without the unmodeled sources of bias, and with and without the imposition of the scale cuts. These results are shown in Fig. 5. For ease of visualization, we show the shifts in the posteriors only in the space of Ω_M and S_8. These two cosmological parameters are tightly constrained by the 3×2pt and 5×2pt analysis, and so are particularly useful for assessing the effectiveness of our scale cut choices. The left panel of Fig. 5 shows the constraints on Ω_m and S_8 obtained when analyzing the simulated data vectors with and without the unmodeled effects when all scales are included in the analysis of $w^{\delta_g\kappa_{\rm CMB}}(\theta)$ and $w^{\gamma_t\kappa_{\rm CMB}}(\theta)$ (but imposing the fiducial scale cuts on the 3×2pt subset of the data vector). In this case, the bias induced by the unmodeled effects is unacceptably large, significantly greater than the statistical uncertainties. The right panel of Fig. 5 shows the cosmological constraints when small scales are excluded as described above. In this case, the bias is significantly reduced at the cost of larger error bars. We find that the shift in the mean S_8 due to the unmodeled effects is 43% of the statistical uncertainty on S_8, which we deem acceptably small. The shift in the mean Ω_M is 35%. We also note that with the scale cuts imposed, Ω_m appears to be degenerate with S_8, while they are much less degenerate without the scale cuts. This implies that the additional small-scale power in the $w^{\gamma_t\kappa_{\rm CMB}}(\theta)$ and $w^{\delta_g\kappa_{\rm CMB}}(\theta)$ measurements helps to break this degen-

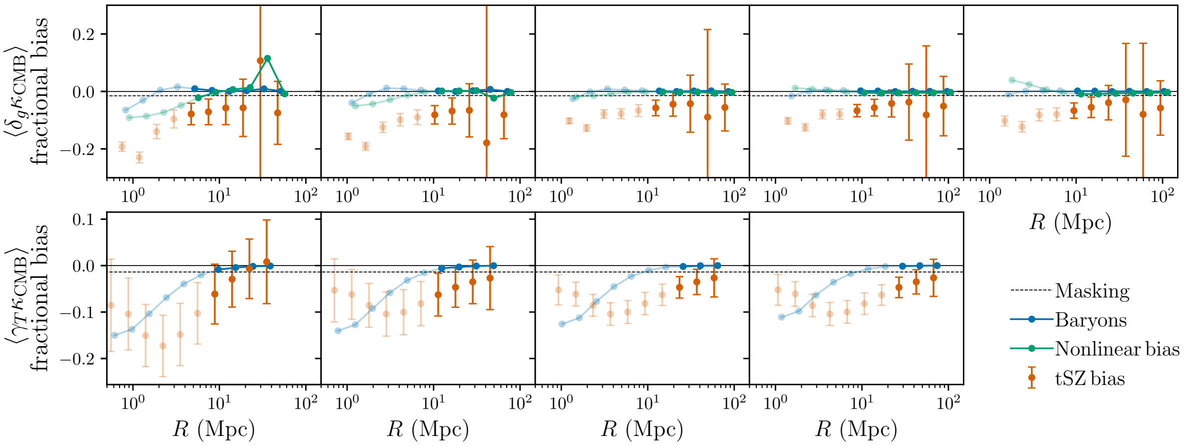

Figure 4. Biases in $w^{\gamma_t\kappa_{\rm CMB}}(\theta)$ and $w^{\delta_g\kappa_{\rm CMB}}(\theta)$ relative to the error bars as a function of physical separation. Faded points are excluded by scale cuts. Errorbars correspond to 10% of the square root of the diagonal of the covariance matrix described in §3.3; for ease of visualization, we only plot errorbars on the tSZ-biased points. The dashed line labeled 'Masking' refers to the roughly 1% bias induced by masking galaxy clusters described in §4.4.

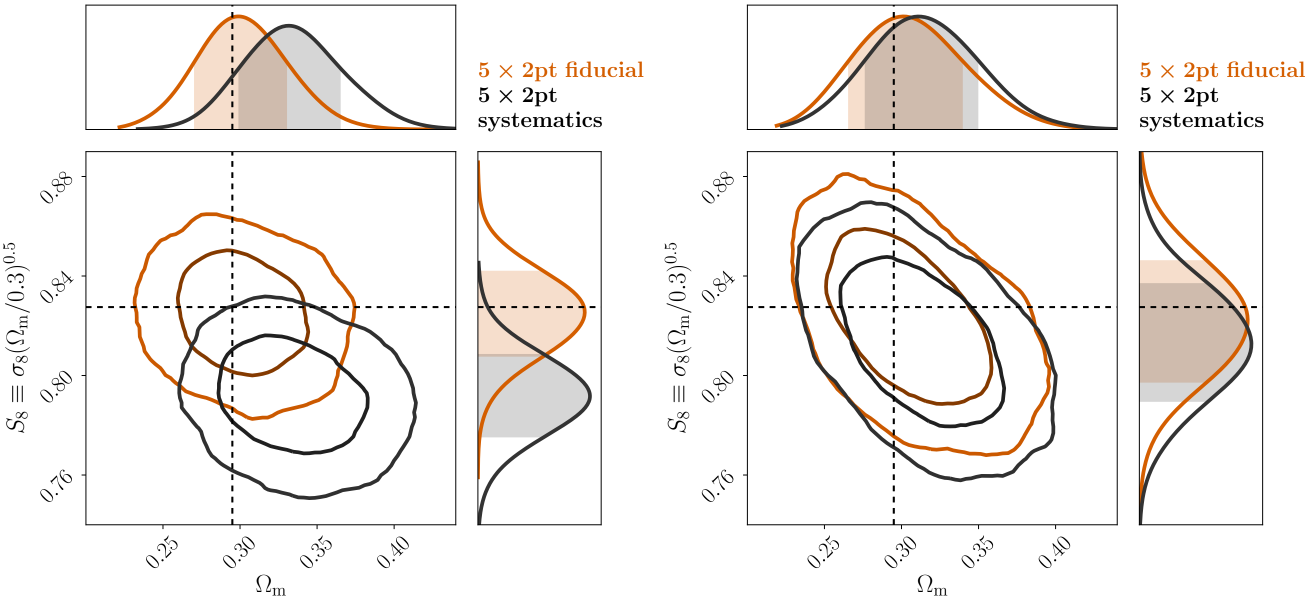

Figure 5. Effects on cosmological constraints of unmodeled contributions to the simulated data vector before (left) and after (right) the application of angular scale cuts on $w^{\delta_g\kappa_{\rm CMB}}(\theta)$ and $w^{\gamma_t\kappa_{\rm CMB}}(\theta)$. 'Fiducial' refers to the data vector generated using the baseline model described in §3; 'Systematics' refers to the simulated data vector that includes prescriptions for tSZ bias in the $\kappa_{\rm CMB}$ map, nonlinear galaxy bias, and the OWLS AGN model for baryons. The scale cuts applied to the 3×2pt subset of observables are kept fixed throughout to those of DES Collaboration et al. (2017).

eracy. Note that the residual bias exhibited in the right panel of Fig. 5 is partially due to the effects of nonlinear galaxy bias and baryons on the 3×2pt combination of observables. The total $\Delta\chi^2$ between the biased and fiducial 5×2pt data vectors is 0.81. Of this, 0.45 is contributed by $w^{\delta_g\kappa_{\rm CMB}}(\theta)$ and $w^{\gamma_t\kappa_{\rm CMB}}(\theta)$. One could in principle make the 3×2pt scale cuts more conservative in order to relax the scale cuts on $w^{\delta_g\kappa_{\rm CMB}}(\theta)$ and $w^{\gamma_t\kappa_{\rm CMB}}(\theta)$ somewhat. However, we have not taken this approach in order to maintain consistency with the analysis of DES Collaboration et al. (2017).

We note that our choice of scale cuts removes a significant fraction of the signal-to-noise in $w^{\gamma_t\kappa_{\rm CMB}}(\theta)$ and $w^{\delta_g\kappa_{\rm CMB}}(\theta)$, resulting in significantly degraded cosmological constraints from these two correlation functions. However, given that we use the $\kappa_{\rm CMB}$ maps from Omori et al. (2017), this choice seems unavoidable. For future work, reducing tSZ leakage into the $\kappa_{\rm CMB}$ maps is a high priority. Alternatively, it may be possible to model the effects of tSZ bias in the analysis.

6 RESULTS OF SIMULATED ANALYSES

Having described our model for the 5×2pt combination of observables and our choice of angular scale cuts, we now present the results of simulated likelihood analyses. For this purpose, we use the simulated data vector described in §5. The simulated data vector is

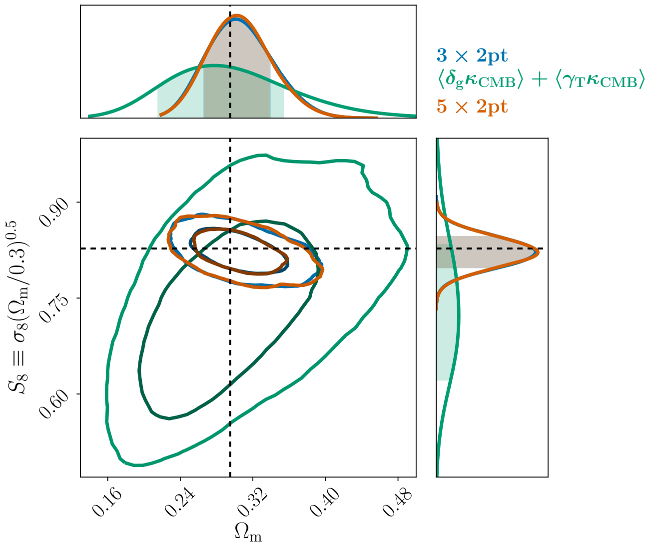

Figure 6. Constraints on $\Omega_{\rm m}$ and S_8 for 3×2pt (red), 5×2pt (blue), and the two 2pt function that cross-correlation with the CMB lensing map, $w^{\delta_g\kappa_{\rm CMB}}(\theta)$ and $w^{\gamma_t\kappa_{\rm CMB}}(\theta)$ (green). The dashed black line shows the fiducial values of $\Omega_{\rm m}$ and S_8.

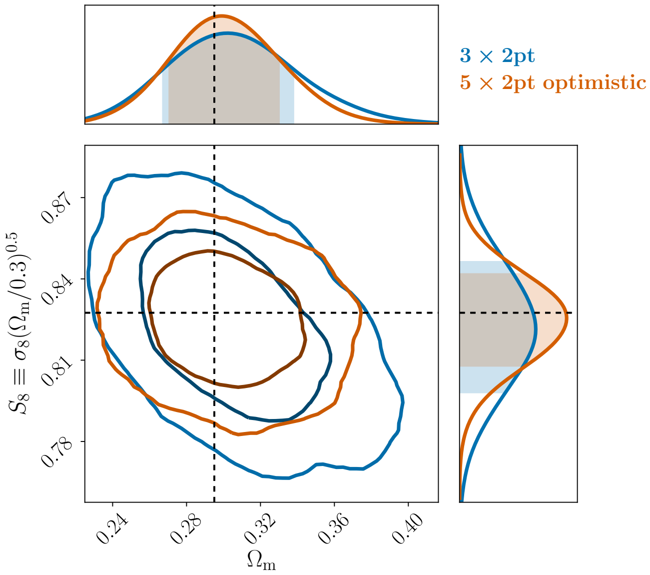

Figure 7. Constraints on $\Omega_{\rm m}$ and S_8 for 3×2pt (red) and 5×2pt (blue) when no scale cuts are applied to the analysis. The dashed black line shows the fiducial values of $\Omega_{\rm m}$ and S_8.

generated without noise so that — by definition — the maximum likelihood point occurs at the true parameter values.

6.1 Fiducial results

We first present projected constraints on cosmological parameters generated from our analysis of a simulated 5×2pt data vector assuming the fiducial choice of angular scale cuts described in §5. Fig. 6 shows the constraints on $\Omega_{\rm m}$ and S_8 generated from our fiducial analysis under the ΛCDM model. Also shown in Fig. 6 is the constraint coming from the joint analysis of $w^{\delta_g\kappa_{\rm CMB}}(\theta)$ and $w^{\gamma_t\kappa_{\rm CMB}}(\theta)$ alone. Given the current errorbars, the constraining power of $w^{\delta_g\kappa_{\rm CMB}}(\theta)$ and $w^{\gamma_t\kappa_{\rm CMB}}(\theta)$ is significantly weaker than that of the 3×2pt combination. This is not too surprising given the low signal-to-noise of the $w^{\delta_g\kappa_{\rm CMB}}(\theta)$ and $w^{\gamma_t\kappa_{\rm CMB}}(\theta)$ correlation functions after the imposition of scale cuts: the combined signal-to-noise from these observables is roughly 8.8. The signal-to-noise of the 3×2pt combination after imposing scale cuts, on the other hand, is approximately 41. Consequently, extending 3×2pt to 5×2pt does not have a dramatic impact in terms of tightening cosmological constraints. Interestingly, though, the degeneracy direction of the combined $w^{\delta_g\kappa_{\rm CMB}}(\theta)$ and $w^{\gamma_t\kappa_{\rm CMB}}(\theta)$ constraint in the S_8–$\Omega_{\rm m}$ parameter space is very complementary to that of the 3×2pt analysis.

Ignoring the effects of tSZ, nonlinear galaxy bias, and baryons, the projected signal-to-noise of the 5×2pt analysis including all angular bins is 20. After the fiducial scale cuts are imposed, the signal-to-noise is reduced to 8.8. An interesting question to ask, then, is how well could the 5×2pt combination constrain cosmology if all of the original signal to noise could be exploited? Fig. 7 shows the cosmological constraints from the 5×2pt analysis on S_8 and $\Omega_{\rm m}$ when no scale cuts are imposed on $w^{\delta_g\kappa_{\rm CMB}}(\theta)$ and $w^{\gamma_t\kappa_{\rm CMB}}(\theta)$. In this case, the 5×2pt analysis significantly shrinks the constraint contour. We note that this figure is meant simply to illustrate the potential signal-to-noise of the cross-correlations between DES Y1 data and the $\kappa_{\rm CMB}$ maps. The result is overly optimistic because it ignores other sources of model bias (i.e. baryons, nonlinear galaxy bias, etc.). As shown in Fig. 4, other sources of model bias can become significant at small scales. All results presented below will use the fiducial choice of scale cuts described in §5.

6.2 Self-calibration of systematics parameters

In addition to the cosmological parameters, there are many nuisance parameters varied in this analysis, including m_i, Δz_s, the galaxy bias, and intrinsic alignment parameters. One of the main advantages of joint two-point function analyses is that the resultant cosmological constraints are quite robust to such nuisance parameters (e.g. Hu & Jain 2004). This is not true for the analysis of single 2pt functions. For example, fits to $w^{\delta_g\gamma_t}(\theta)$ alone lead to complete degeneracy between galaxy bias and A_s, while fits to $w^{\gamma\gamma}(\theta)$ lead to a complete degeneracy between m and A_s. Many of these degeneracies are broken by the 3×2pt combination of observables, since there is no nuisance parameter that affects $w^{\delta_g\delta_g}(\theta)$, $w^{\delta_g\gamma}(\theta)$, and $w^{\gamma\gamma}(\theta)$ in the same way. For instance, $w^{\delta_g\gamma}(\theta)$ scales with the shear calibration bias as $(1+m)$, $w^{\gamma\gamma}(\theta)$ scales with $(1+m)^2$, but $w^{\delta_g\delta_g}(\theta)$ is independent of $(1+m)$.

However, even the 3×2pt analysis of DES Collaboration et al. (2017) is not completely immune to degeneracies between nuisance parameters and cosmological parameters. In particular, the cosmological constraints of the 3×2pt analysis are degraded by a three-parameter degeneracy between galaxy bias, shear calibration, and A_s. Consider the effect of increasing the galaxy bias, b, by some factor $\alpha > 1$ such that $b \rightarrow \alpha b$. In that case, the amplitude of $w^{\delta_g\gamma}(\theta)$ will increase by α and $w^{\delta_g\delta_g}(\theta)$ will increase by α^2, while $w^{\gamma\gamma}(\theta)$ remains unchanged. These changes can be compensated partly by decreasing A_s by α^2, which will result in $w^{\gamma\gamma}(\theta)$ decreasing by α^2, $w^{\delta_g\gamma}(\theta)$ being reduced by α relative to its original value, and $w(\theta)$ returning to its original value. Finally, if shear calibration, m, is increased such that $(1+m) \rightarrow \alpha(1+m)$, then $w^{\delta_g\gamma}(\theta)$ and $w(\theta)$ will return to their original values. The net result is a counterintuitive *positive* correlation between m and galaxy bias. This degen-

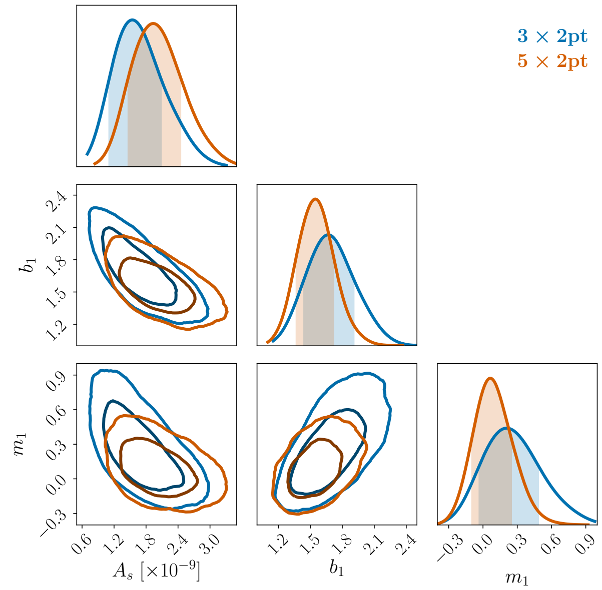

Figure 8. Illustration of the degeneracy between A_s, galaxy bias (b_1) and shear bias (m_1) in the 3×2pt and 5×2pt analyses. For this figure, we have placed very wide and flat priors on the shear calibration parameters.

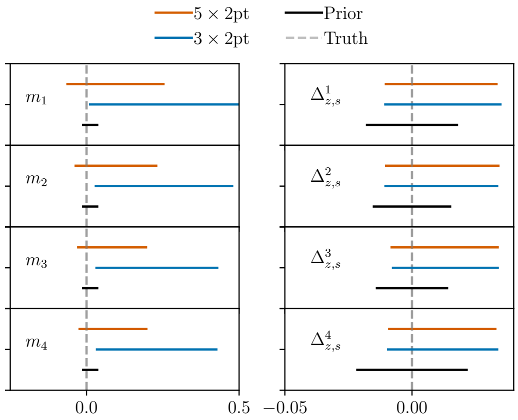

Figure 9. Recovered constraints (68% confidence interval) on multiplicative shear bias (left) and photometric redshift bias (right) for the 5×2pt analysis (orange bars) and 3×2pt analysis (blue bars) when the priors on these parameters are completely non-informative. Black bars show the priors imposed on the m_i in the fiducial analysis.

eracy is illustrated for a single redshift bin with the blue contours in Fig. 8. Since the fiducial priors on m significantly restrict its allowed range, it is hard to see the degeneracy between m and other parameters when these priors are imposed. Consequently, when generating Fig. 8 we have replaced the fiducial m prior with one that is flat over the range $m \in [-1, 1]$.

As a result of the above degeneracy in the 3×2pt analysis, it is useful to impose informative priors on the multiplicative bias parameters and the redshift bias parameters. For the DES Collaboration et al. (2017) analysis, the priors on multiplicative shear bias for the METACALIBRATION catalog are derived using a variety of tests described in Zuntz et al. (2017). In the case of redshift biases, priors on the source redshift biases are derived using comparisons to data from the COSMOS (Laigle et al. 2016) field in Hoyle et al. (2017) and angular clustering in Davis et al. (2017) and Gatti et al. (2017). While such priors are believed to be robust, they are difficult to obtain, require data external to the correlation function measurements, and in the case of shear bias, rely on image simulations which may not exactly match the data[5]. Because of these challenges and associated uncertainties, it would be advantageous if the correlation function measurements themselves could break the nuisance parameter degeneracies, and *self-calibrate* m and Δz_s.

As pointed out by several authors (e.g. Vallinotto 2012; Baxter et al. 2016; Liu et al. 2016; Schaan et al. 2017) joint measurements of galaxy lensing and CMB lensing correlations can enable self-calibration of both multiplicative shear bias and photometric redshift biases. This is possible because CMB lensing and galaxy lensing are correlated, while CMB lensing is not sensitive to these two sources of systematic error, thus breaking the three-parameter degeneracy between shear bias, galaxy bias, and A_s described above.[6] This degeneracy breaking is illustrated with the red contours in Fig. 8. In fact, either one of $w^{\delta_g \kappa_{\rm CMB}}(\theta)$ or $w^{\gamma_t \kappa_{\rm CMB}}(\theta)$ is sufficient to break this degeneracy. The $w^{\gamma_t \kappa_{\rm CMB}}(\theta)$ correlation breaks this degeneracy because this quantity depends on m, but not on galaxy bias; it is broken by $w^{\delta_g \kappa_{\rm CMB}}(\theta)$ because this quantity depends on galaxy bias, but not on m.

We now investigate the potential of the 5×2pt analysis to self-calibrate the shear and photo-z bias parameters by replacing the fiducial priors on these parameters (in Table 1) with very wide and flat priors. For m, we use $m \in [-1, 1]$; for Δz_s, we use $\Delta z_s \in [-1, 1]$.

The posteriors on the shear calibration parameters resulting from the 5×2pt and 3×2pt analyses for wide priors on m are summarized in the left panel of Fig. 9. The blue bands in that figure illustrate the level at which the 3×2pt combination is able to self-calibrate the multiplicative shear bias, roughly $\sigma(m) \sim 0.2$. Note that the confidence intervals shown in Fig. 9 are not centered on the input shear values, even though the maximum likelihood point in the full parameter space does occur at the input parameter values; this is simply the result of projecting the higher dimensional parameter space to the 1D parameter space shown in the figure. We find that the 5×2pt combination is able to significantly improve on the self-calibration of m, reaching constraints of roughly $\sigma(m) \sim 0.1$, with the constraints improved somewhat for higher redshift bins (orange bands). This level of shear calibration is certainly interesting, but is not yet competitive with priors on the m obtained in the fiducial DES Collaboration et al. (2017) 3×2pt analysis (black bands).

Changing the priors on Δz_s to be flat reveals that the 5×2pt analysis constrains these biases at roughly $\sigma(\Delta z_s) \sim 0.03 - 0.04$ (right panel of Fig. 9). This level of constraint is only a factor of ~ 2 weaker than the fiducial priors on Δz_s. However, we find that the posterior on Δz_s from the 3×2pt analysis is almost identical to that from 5×2pt. The reason for this is that Δz_s is not impacted by the three parameter degeneracy that affects m in the 3×2pt analysis, and can therefore be tightly constrained using 3×2pt alone.

The constraints on Ω_m and S_8 obtained from the 3×2pt and 5×2pt analyses when the priors on m are very wide and flat are shown in Fig. 10. This figure highlights the exciting potential of

---

[5] As described in Section 5 of Zuntz et al. (2017), the residual shear calibration bias in METACALIBRATION from PSF modeling errors is determined using image simulations, even though the METACALIBRATION algorithm itself does not require simulations.

[6] In principle, CMB lensing could also have some form of multiplicative bias. However, for current measurements, any multiplicative bias is expected to be much smaller than the associated statistical errorbars.

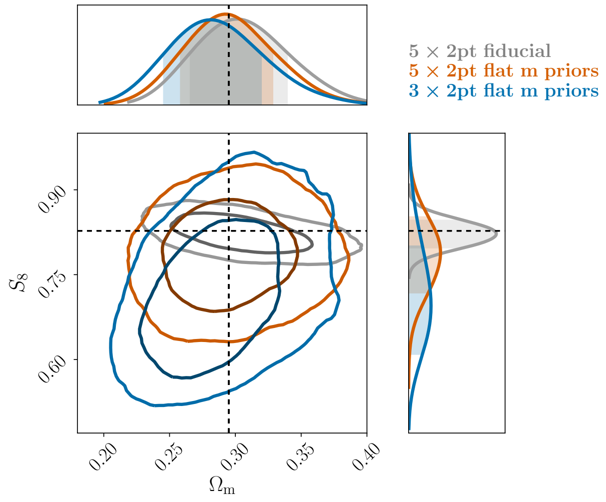

Figure 10. Constraints on $\Omega_{\rm m}$, S_8 with and without fiducial priors on shear calibration bias. With non-informative priors on shear calibration bias, the 5×2pt analysis is able to obtain tight cosmological constraints. The 3×2pt analysis, however, is significantly degraded in the absence of tight priors on shear calibration.

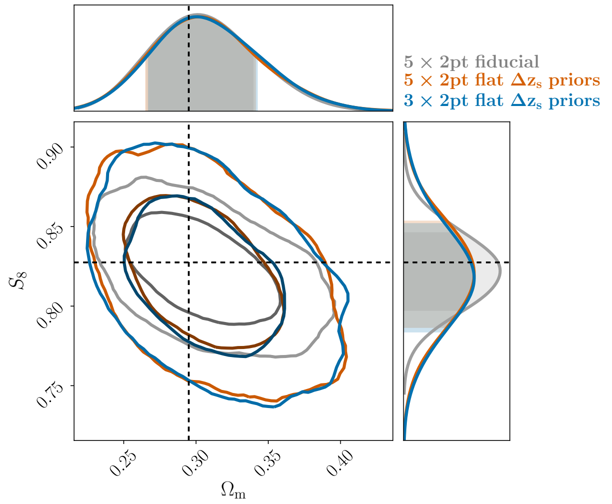

Figure 11. Constraints on $\Omega_{\rm m}$, S_8 with and without priors on source photometric redshift bias.

the 5×2pt analysis: with a non-informative prior on m, the 5×2pt analysis can obtain significantly tighter cosmological constraints than the 3×2pt analysis. We see that weakening the priors on m mostly degrades the cosmological constraints in the S_8 direction. This is because S_8 effectively controls the amplitude of the correlation functions, and its is thus strongly impacted by the degeneracy between shear calibration, galaxy bias, and A_s described above. Also shown in Fig. 10 are the contours obtained from the 5×2pt analysis with the fiducial m priors. Comparing these contours to those with the loose m priors reveals that the priors on m do contribute some information to the cosmological constraints. This is not surprising, given that the level at which 5×2pt self-calibrates m is significantly looser than the fiducial priors on m. Fig. 11 shows the cosmological constraints obtained from the 5×2pt and 3×2pt analyses when the priors on Δz_s become non-informative. In this case, we see little improvement of the 5×2pt combination relative to the 3×2pt combination. We find that the fiducial priors on Δz_s are useful for improving cosmological constraints in the 5×2pt analysis, indicating that the data is not self-calibrating for this parameter.

7 DISCUSSION

We have presented the methodology for jointly analyzing the combination of five two-point functions that can be formed from the combination of the δ_g, γ and $\kappa_{\rm CMB}$ observables (not including the $\kappa_{\rm CMB}$ autocorrelation). This methodology will be applied to a forthcoming analysis using data from DES, SPT and *Planck*.

Essential to this analysis is the characterization of the bias in maps of $\kappa_{\rm CMB}$ induced by the thermal Sunyaev-Zel'dovich effect. Our estimate of this bias suggests that it could be quite large at small scales. Given the uncertainties associated with this estimate, we do not attempt to model tSZ bias in our analysis. Instead, we remove angular scales that are estimated to be strongly affected by the bias, at the cost of increasing our statistical errorbars. This degradation is significant: the total expected signal-to-noise of the $w^{\gamma_t\kappa_{\rm CMB}}(\theta)$ and $w^{\delta_g\kappa_{\rm CMB}}(\theta)$ cross-correlations is roughly 20; after the scale cuts, this is reduced to 8.8.

Given the scale cuts required to remove tSZ contamination of the $\kappa_{\rm CMB}$ maps, we find that the joint cosmological constraining power of $w^{\delta_g\kappa_{\rm CMB}}(\theta)$ and $w^{\gamma_t\kappa_{\rm CMB}}(\theta)$ is significantly weaker than the 3×2pt analysis (Fig. 6). Consequently, the 5×2pt analysis does not lead to dramatic improvement in cosmological constraints given the fiducial priors of the 3×2pt analysis.

However, we find that the 5×2pt analysis can significantly improve on the cosmological constraining power of the 3×2pt analysis in the case that priors on the multiplicative shear biases are loosened. As shown in Fig. 10, with essentially no information on the multiplicative bias parameters, the 5×2pt analysis can still obtain tight cosmological constraints.

Given the large degradation in signal-to-noise that results from cutting scales affected by tSZ contamination, future work to model or remove such contamination is strongly motivated. More accurate estimates of the contamination could be achieved with high signal-to-noise and high resolution Compton y maps. Alternatively, such contamination could be removed from the $\kappa_{\rm CMB}$ maps using either multi-frequency component separation methods to remove tSZ from the CMB temperature maps, or by constructing the $\kappa_{\rm CMB}$ maps instead from maps of the CMB polarization, since the tSZ signal is nearly unpolarized.

ACKNOWLEDGEMENTS

This paper has gone through internal review by the DES collaboration.

EB is partially supported by the US Department of Energy grant DE-SC0007901. The Melbourne group acknowledges support from the Australian Research Council's Future Fellowships scheme (FT150100074). PF is funded by MINECO, projects ESP2013-48274-C3-1-P, ESP2014-58384-C3-1-P, and ESP2015-66861-C3-1-R. ER is supported by DOE grant DE-SC0015975 and by the Sloan Foundation, grant FG- 2016-6443.

Funding for the DES Projects has been provided by the U.S. Department of Energy, the U.S. National Science Foundation, the Ministry of Science and Education of Spain, the Science and Technology Facilities Council of the United Kingdom, the

Higher Education Funding Council for England, the National Center for Supercomputing Applications at the University of Illinois at Urbana-Champaign, the Kavli Institute of Cosmological Physics at the University of Chicago, the Center for Cosmology and Astro-Particle Physics at the Ohio State University, the Mitchell Institute for Fundamental Physics and Astronomy at Texas A&M University, Financiadora de Estudos e Projetos, Fundação Carlos Chagas Filho de Amparo à Pesquisa do Estado do Rio de Janeiro, Conselho Nacional de Desenvolvimento Científico e Tecnológico and the Ministério da Ciência, Tecnologia e Inovação, the Deutsche Forschungsgemeinschaft and the Collaborating Institutions in the Dark Energy Survey.

The Collaborating Institutions are Argonne National Laboratory, the University of California at Santa Cruz, the University of Cambridge, Centro de Investigaciones Energéticas, Medioambientales y Tecnológicas-Madrid, the University of Chicago, University College London, the DES-Brazil Consortium, the University of Edinburgh, the Eidgenössische Technische Hochschule (ETH) Zürich, Fermi National Accelerator Laboratory, the University of Illinois at Urbana-Champaign, the Institut de Ciències de l'Espai (IEEC/CSIC), the Institut de Física d'Altes Energies, Lawrence Berkeley National Laboratory, the Ludwig-Maximilians Universität München and the associated Excellence Cluster Universe, the University of Michigan, the National Optical Astronomy Observatory, the University of Nottingham, The Ohio State University, the University of Pennsylvania, the University of Portsmouth, SLAC National Accelerator Laboratory, Stanford University, the University of Sussex, Texas A&M University, and the OzDES Membership Consortium.

Based in part on observations at Cerro Tololo Inter-American Observatory, National Optical Astronomy Observatory, which is operated by the Association of Universities for Research in Astronomy (AURA) under a cooperative agreement with the National Science Foundation.

The DES data management system is supported by the National Science Foundation under Grant Numbers AST-1138766 and AST-1536171. The DES participants from Spanish institutions are partially supported by MINECO under grants AYA2015-71825, ESP2015-88861, FPA2015-68048, SEV-2012-0234, SEV-2016-0597, and MDM-2015-0509, some of which include ERDF funds from the European Union. IFAE is partially funded by the CERCA program of the Generalitat de Catalunya. Research leading to these results has received funding from the European Research Council under the European Union's Seventh Framework Program (FP7/2007-2013) including ERC grant agreements 240672, 291329, and 306478. We acknowledge support from the Australian Research Council Centre of Excellence for All-sky Astrophysics (CAASTRO), through project number CE110001020.

This manuscript has been authored by Fermi Research Alliance, LLC under Contract No. DE-AC02-07CH11359 with the U.S. Department of Energy, Office of Science, Office of High Energy Physics. The United States Government retains and the publisher, by accepting the article for publication, acknowledges that the United States Government retains a non-exclusive, paid-up, irrevocable, world-wide license to publish or reproduce the published form of this manuscript, or allow others to do so, for United States Government purposes.

The South Pole Telescope program is supported by the National Science Foundation through grant PLR-1248097. Partial support is also provided by the NSF Physics Frontier Center grant PHY-0114422 to the Kavli Institute of Cosmological Physics at the University of Chicago, the Kavli Foundation, and the Gordon and Betty Moore Foundation through Grant GBMF#947 to the University of Chicago. Argonne National LaboratoryâĂŹs work was supported under the U.S. Department of Energy contract DE-AC02-06CH11357.

Argonne National Laboratory work was supported under U.S. Department of Energy contract DE-AC02-06CH11357.

REFERENCES

Abbott T., et al., 2016, Phys. Rev., D94, 022001
Arnaud M., Pratt G. W., Piffaretti R., Böhringer H., Croston J. H., Pointecouteau E., 2010, A&A, 517, A92
Baldauf T., Seljak U., Desjacques V., McDonald P., 2012, Phys. Rev. D, 86, 083540
Bartelmann M., Schneider P., 2001, Phys. Rep., 340, 291
Battaglia N., Bond J. R., Pfrommer C., Sievers J. L., 2012, ApJ, 758, 75
Baxter E., et al., 2016, MNRAS, 461, 4099
Bird S., Viel M., Haehnelt M. G., 2012, MNRAS, 420, 2551
Blanton M. R., Eisenstein D., Hogg D. W., Zehavi I., 2006, ApJ, 645, 977
Bleem L. E., et al., 2015, ApJS, 216, 27
Bridle S., King L., 2007, New Journal of Physics, 9, 444
Carlstrom J. E., Holder G. P., Reese E. D., 2002, ARA&A, 40, 643
Carlstrom J. E., et al., 2011, Publications of the Astronomical Society of the Pacific, 123, 568
Catelan P., Porciani C., 2001, MNRAS, 323, 713
Cavaliere A., Fusco-Femiano R., 1976, A&A, 49, 137
Cresswell J. G., Percival W. J., 2009, MNRAS, 392, 682
Crittenden R. G., Natarajan P., Pen U.-L., Theuns T., 2001, ApJ, 559, 552
DES Collaboration et al., 2017, preprint, (`arXiv:1708.01530`)
Das S., Spergel D. N., 2009, Phys. Rev. D, 79, 043509
Das S., Errard J., Spergel D., 2013, preprint, (`arXiv:1311.2338`)
Davis C., et al., 2017, preprint, (`arXiv:1710.02517`)
Drlica-Wagner A., et al., 2017, preprint, (`arXiv:1708.01531`)
Eifler T., Schneider P., Hartlap J., 2009, A&A, 502, 721
Elvin-Poole J., et al., 2017, preprint, (`arXiv:1708.01536`)
Feroz F., Hobson M. P., Bridges M., 2009, MNRAS, 398, 1601
Foreman-Mackey D., Hogg D. W., Lang D., Goodman J., 2013, PASP, 125, 306
Gatti M., et al., 2017, preprint, (`arXiv:1709.00992`)
George E. M., et al., 2015, ApJ, 799, 177
Giannantonio T., et al., 2016, MNRAS, 456, 3213
Goodman J., Weare J., 2010, Communications in Applied Mathematics and Computational Science, Vol.~5, No.~1, p.~65-80, 2010, 5, 65
Hall A., Taylor A., 2014, MNRAS, 443, L119
Hand N., et al., 2015, Phys. Rev. D, 91, 062001
Harnois-Déraps J., et al., 2016, MNRAS, 460, 434
Harnois-Déraps J., et al., 2017, preprint, (`arXiv:1703.03383`)
Heavens A., Refregier A., Heymans C., 2000, MNRAS, 319, 649
Hildebrandt H., et al., 2017, MNRAS, 465, 1454
Hirata C. M., Seljak U., 2004, Phys. Rev. D, 70, 063526
Howlett C., Lewis A., Hall A., Challinor A., 2012, J. Cosmology Astropart. Phys., 4, 027
Hoyle B., et al., 2017, preprint, (`arXiv:1708.01532`)
Hu W., Jain B., 2004, Phys. Rev. D, 70, 043009
Hu W., Okamoto T., 2002, ApJ, 574, 566
Huff E., Mandelbaum R., 2017, preprint, (`arXiv:1702.02600`)
Joudaki S., et al., 2017, MNRAS, 465, 2033
Kirk D., et al., 2016, MNRAS, 459, 21
Krause E., Eifler T., 2017, MNRAS, 470, 2100
Krause E., et al., 2017, preprint, (`arXiv:1706.09359`)
Kwan J., et al., 2017, MNRAS, 464, 4045
Laigle C., et al., 2016, ApJS, 224, 24
Lewis A., Challinor A., Lasenby A., 2000, ApJ, 538, 473
Limber D. N., 1953, ApJ, 117, 134
Liu J., Ortiz-Vazquez A., Hill J. C., 2016, Phys. Rev. D, 93, 103508
McDonald P., Roy A., 2009, J. Cosmology Astropart. Phys., 8, 020

McEwen J. E., Fang X., Hirata C. M., Blazek J. A., 2016, J. Cosmology Astropart. Phys., 9, 015
Melchior P., et al., 2017, MNRAS, 469, 4899
Morrison C. B., Schneider M. D., 2013, J. Cosmology Astropart. Phys., 11, 009
Navarro J. F., Frenk C. S., White S. D. M., 1996, ApJ, 462, 563
Nicola A., Refregier A., Amara A., 2016, Phys. Rev. D, 94, 083517
Omori Y., et al., 2017, The Astrophysical Journal, 849, 124
Planck Collaboration et al., 2011, A&A, 536, A1
Planck Collaboration et al., 2016a, A&A, 594, A15
Planck Collaboration et al., 2016b, A&A, 594, A22
Planck Collaboration et al., 2016c, A&A, 594, A24
Planck Collaboration et al., 2016d, A&A, 594, A27
Planck Collaboration et al., 2016e, A&A, 596, A109
Prat J., et al., 2017, preprint, (`arXiv:1708.01537`)
Rozo E., et al., 2016, MNRAS, 461, 1431
Rykoff E. S., et al., 2014, ApJ, 785, 104
Rykoff E. S., et al., 2016, ApJS, 224, 1
Saro A., et al., 2017, MNRAS, 468, 3347
Schaan E., Krause E., Eifler T., Doré O., Miyatake H., Rhodes J., Spergel D. N., 2017, Phys. Rev. D, 95, 123512
Schaye J., et al., 2010, MNRAS, 402, 1536
Sheldon E. S., Huff E. M., 2017, ApJ, 841, 24
Smith R. E., et al., 2003, MNRAS, 341, 1311
Story K. T., et al., 2013, ApJ, 779, 86
Takada M., Hu W., 2013, Phys. Rev. D, 87, 123504
Takahashi R., Sato M., Nishimichi T., Taruya A., Oguri M., 2012, ApJ, 761, 152
Tauber J. A., et al., 2010, A&A, 520, A1
Troxel M. A., Ishak M., 2014, Phys. Rev. D, 89, 063528
Troxel M. A., et al., 2017, preprint, (`arXiv:1708.01538`)
Vallinotto A., 2012, ApJ, 759, 32
Zehavi I., et al., 2005, ApJ, 630, 1
Zuntz J., Kacprzak T., Voigt L., Hirsch M., Rowe B., Bridle S., 2013, MNRAS, 434, 1604
Zuntz J., et al., 2015, Astronomy and Computing, 12, 45
Zuntz J., et al., 2017, preprint, (`arXiv:1708.01533`)
van Engelen A., Bhattacharya S., Sehgal N., Holder G. P., Zahn O., Nagai D., 2014, ApJ, 786, 13
van Uitert E., et al., 2017, preprint, (`arXiv:1706.05004`)

APPENDIX A: AFFILIATIONS

[1] *Department of Physics and Astronomy, University of Pennsylvania, Philadelphia, PA 19104, USA*
[2] *Kavli Institute for Particle Astrophysics and Cosmology, Stanford University, 452 Lomita Mall, Stanford, CA 94305*
[3] *Dept. of Physics, Stanford University, 382 Via Pueblo Mall, Stanford, CA 94305*
[4] *Department of Physics and McGill Space Institute, McGill University, Montreal, Quebec H3A 2T8, Canada*
[5] *Kavli Institute for Cosmological Physics, University of Chicago, 5640 South Ellis Avenue, Chicago, IL 60637, USA*
[6] *Institute of Astronomy, University of Cambridge, Madingley Road, Cambridge CB3 0HA, UK*
[7] *Kavli Institute for Cosmology, University of Cambridge, Madingley Road, Cambridge CB3 0HA, UK*
[8] *Universitäts-Sternwarte, Fakultät für Physik, Ludwig-Maximilians Universität München, Scheinerstr. 1, 81679 München, Germany*
[9] *Department of Physics & Astronomy, University College London, Gower Street, London, WC1E 6BT, UK*
[10] *Department of Astronomy/Steward Observatory, 933 North Cherry Avenue, Tucson, AZ 85721-0065, USA*
[11] *Jet Propulsion Laboratory, California Institute of Technology, 4800 Oak Grove Dr., Pasadena, CA 91109, USA*
[12] *Center for Cosmology and Astro-Particle Physics, The Ohio State University, Columbus, OH 43210, USA*
[13] *Institute of Physics, Laboratory of Astrophysics, École Polytechnique Fédérale de Lausanne (EPFL), Observatoire de Sauverny, 1290 Versoix, Switzerland*
[14] *Department of Physics, University of Chicago, 5640 South Ellis Avenue, Chicago, IL 60637, USA*
[15] *Argonne National Laboratory, 9700 South Cass Avenue, Lemont, IL 60439, USA*
[16] *Fermi National Accelerator Laboratory, P. O. Box 500, Batavia, IL 60510, USA*
[17] *Scottish Universities Physics Alliance, Institute for Astronomy, University of Edinburgh, Royal Observatory, Blackford Hill, Edinburgh, EH9 3HJ, UK*
[18] *Center for Cosmology and AstroParticle Physics, The Ohio State University, 191 West Woodruff Avenue, Columbus, OH 43210, USA*
[19] *Department of Astronomy and Astrophysics, University of Chicago, Chicago, IL 60637, USA*
[20] *Observatories of the Carnegie Institution of Washington, 813 Santa Barbara St., Pasadena, CA 91101, USA*
[21] *Kavli Institute for Particle Astrophysics & Cosmology, P. O. Box 2450, Stanford University, Stanford, CA 94305, USA*
[22] *SLAC National Accelerator Laboratory, Menlo Park, CA 94025, USA*
[23] *Canadian Institute for Advanced Research, CIFAR Program on Gravity and the Extreme Universe, Toronto, ON, M5G 1Z8, Canada*
[24] *Astronomy Department, University of Illinois at Urbana Champaign, 1002 W. Green Street, Urbana, IL 61801, USA*
[25] *Department of Physics, University of Illinois Urbana Champaign, 1110 W. Green Street, Urbana, IL 61801, USA*
[26] *Department of Physics, The Ohio State University, Columbus, OH 43210, USA*
[27] *Department of Physics, ETH Zurich, Wolfgang-Pauli-Strasse 16, CH-8093 Zurich, Switzerland*
[28] *Institut de Física d'Altes Energies (IFAE), The Barcelona Institute of Science and Technology, Campus UAB, 08193 Bellaterra (Barcelona) Spain*
[29] *School of Physics, University of Melbourne, Parkville, VIC 3010, Australia*
[30] *Jodrell Bank Center for Astrophysics, School of Physics and Astronomy, University of Manchester, Oxford Road, Manchester, M13 9PL, UK*
[31] *Brookhaven National Laboratory, Bldg 510, Upton, NY 11973, USA*
[32] *Institute for Astronomy, University of Edinburgh, Edinburgh EH9 3HJ, UK*
[33] *Cerro Tololo Inter-American Observatory, National Optical Astronomy Observatory, Casilla 603, La Serena, Chile*
[34] *Department of Physics and Electronics, Rhodes University, PO Box 94, Grahamstown, 6140, South Africa*
[35] *Institute of Cosmology & Gravitation, University of Portsmouth, Portsmouth, PO1 3FX, UK*
[36] *LSST, 933 North Cherry Avenue, Tucson, AZ 85721, USA*
[37] *CNRS, UMR 7095, Institut d'Astrophysique de Paris, F-75014, Paris, France*
[38] *Sorbonne Universités, UPMC Univ Paris 06, UMR 7095, Institut d'Astrophysique de Paris, F-75014, Paris, France*
[39] *Laboratório Interinstitucional de e-Astronomia - LIneA, Rua Gal. José Cristino 77, Rio de Janeiro, RJ - 20921-400, Brazil*

[40] *Observatório Nacional, Rua Gal. José Cristino 77, Rio de Janeiro, RJ - 20921-400, Brazil*
[41] *Department of Astronomy, University of Illinois at Urbana-Champaign, 1002 W. Green Street, Urbana, IL 61801, USA*
[42] *National Center for Supercomputing Applications, 1205 West Clark St., Urbana, IL 61801, USA*
[43] *Institut d'Estudis Espacials de Catalunya (IEEC), 08193 Barcelona, Spain*
[44] *Institute of Space Sciences (ICE, CSIC), Campus UAB, Carrer de Can Magrans, s/n, 08193 Barcelona, Spain*
[45] *Centro de Investigaciones Energéticas, Medioambientales y Tecnológicas (CIEMAT), Madrid, Spain*
[46] *George P. and Cynthia Woods Mitchell Institute for Fundamental Physics and Astronomy, and Department of Physics and Astronomy, Texas A&M University, College Station, TX 77843, USA*
[47] *Department of Astronomy, University of Michigan, Ann Arbor, MI 48109, USA*
[48] *Department of Physics, University of Michigan, Ann Arbor, MI 48109, USA*
[49] *Instituto de Fisica Teorica UAM/CSIC, Universidad Autonoma de Madrid, 28049 Madrid, Spain*
[50] *Santa Cruz Institute for Particle Physics, Santa Cruz, CA 95064, USA*
[51] *Max Planck Institute for Extraterrestrial Physics, Giessenbachstrasse, 85748 Garching, Germany*
[52] *Harvard-Smithsonian Center for Astrophysics, Cambridge, MA 02138, USA*
[53] *Australian Astronomical Observatory, North Ryde, NSW 2113, Australia*
[54] *Departamento de Física Matemática, Instituto de Física, Universidade de São Paulo, CP 66318, São Paulo, SP, 05314-970, Brazil*
[55] *Department of Astrophysical Sciences, Princeton University, Peyton Hall, Princeton, NJ 08544, USA*
[56] *Institució Catalana de Recerca i Estudis Avançats, E-08010 Barcelona, Spain*
[57] *School of Physics and Astronomy, University of Southampton, Southampton, SO17 1BJ, UK*
[58] *Center for Particle Astrophysics, Fermi National Accelerator Laboratory, Batavia, IL 60510, USA*
[59] *Instituto de Física Gleb Wataghin, Universidade Estadual de Campinas, 13083-859, Campinas, SP, Brazil*
[60] *Computer Science and Mathematics Division, Oak Ridge National Laboratory, Oak Ridge, TN 37831*
[61] *Excellence Cluster Universe, Boltzmannstr. 2, 85748 Garching, Germany*